

Multimodal Classification Network Guided Trajectory Planning for 4WIS Autonomous Parking Considering Obstacle Attributes

Jingjia Teng, Yang Li, Yougang Bian, *Member, IEEE*, Manjiang Hu, Yingbai Hu, Guofa Li, *Senior Member, IEEE*, Jianqiang Wang

Abstract—Four-wheel Independent Steering (4WIS) vehicles have attracted increasing attention for their superior maneuverability. Human drivers typically choose to cross or drive over the low-profile obstacles (e.g., plastic bags) to efficiently navigate through narrow spaces, while existing planners neglect obstacle attributes, leading to suboptimal efficiency or planning failures. To address this issue, we propose a novel multimodal trajectory planning framework that employs a neural network for scene perception, combines 4WIS hybrid A* search to generate a warm start, and utilizes an optimal control problem (OCP) for trajectory optimization. Specifically, a multimodal perception network fusing visual information and vehicle states is employed to capture semantic and contextual scene understanding, enabling the planner to adapt the strategy according to scene complexity (hard or easy task). For hard tasks, guided points are introduced to decompose complex tasks into local subtasks, improving the search efficiency. The multiple steering modes of 4WIS vehicles—Ackermann, diagonal, and zero-turn—are also incorporated as kinematically feasible motion primitives. Moreover, a hierarchical obstacle handling strategy, which categorizes obstacles as “non-traversable”, “crossable”, and “drive-over”, is incorporated into the node expansion process, explicitly linking obstacle attributes to planning actions to enable efficient decisions. Furthermore, to address dynamic obstacles with motion uncertainty, we introduce a probabilistic risk field model, constructing risk-aware driving corridors that serve as linear collision constraints in OCP. Experimental results demonstrate the proposed framework’s effectiveness in generating safe, efficient, and smooth trajectories for 4WIS vehicles, especially in constrained environments.

Index Terms—4WIS vehicle, trajectory planning, obstacle attributes, driving risk field, optimal control problem.

I. INTRODUCTION

A. Background

FOUR-Wheel Independent Steering (4WIS) vehicles are capable of independently controlling each wheel’s steering angle and have multiple maneuvering modes, including Ackermann steering, diagonal motion, and zero-turn rotation [1]. These diverse motion modes can significantly enhance vehicle maneuverability and improve navigation in narrow environments. Trajectory planning for autonomous vehicles has attracted considerable attention [2], [3], but existing trajectory planning methods often fail to explicitly incorporate these diverse motion capabilities into the planning decision process, thereby limiting their effectiveness in constrained environments [4], [5], [6], limiting their performance in constrained spaces. Besides, most trajectory planning algorithms intend to avoid all obstacles, regardless of the obstacle attributes [7], [8], which not only reduces planning efficiency with “crossable” or “drive-over” obstacles such as tiny rocks,

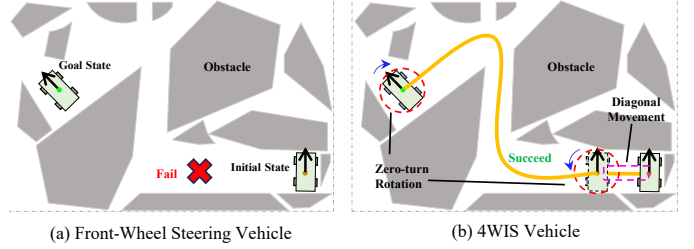


Fig. 1. Trajectory planning of the front-wheel steering vehicle and the 4WIS vehicle. (a) The front-wheel steering vehicle fails to generate a collision-free path due to limited maneuverability. (b) The 4WIS vehicle successfully navigates the narrow space by leveraging multiple motion capabilities.

cardboard boxes, or speed bumps, but also precludes differentiated and interpretable decision-making. Moreover, the motion uncertainty of dynamic obstacles is rarely considered in existing planning frameworks.

This study proposes a novel trajectory planning framework for 4WIS vehicles in narrow and obstacle-dense environments, as illustrated in Fig. 1, accounting for obstacle properties and uncertainty modeling. In Fig. 2, the framework first incorporates a Multimodal Classification Network (MCN) that determines the necessity of guided points, and a Guided Point (GP) generation strategy is developed to assist the hybrid A* algorithm. The 4WIS hybrid A* algorithm integrates multiple kinematic modes through interpretable node expansion and heuristic design, enabling explicit and traceable mode selection during planning. In addition, a hierarchical obstacle handling strategy that accounts for obstacle attributes is implemented to enhance search efficiency. Finally, an optimal control problem (OCP) is formulated, constructing probabilistic risk field-based driving corridors to handle the motion uncertainty of dynamic obstacles and introducing logical constraints for “drive-over” static obstacles. To enhance optimization efficiency, the trajectory generated by the 4WIS hybrid A* serves as a warm start for the trajectory optimization. The main contributions are summarized as follows:

- A multimodal classification network is built to assess the scene complexity (hard/easy) based on the fusion of image and state data. Based on this assessment, a guided point generation strategy is activated for complex scenarios to decompose global planning into interpretable local subtasks, significantly improving the search efficiency.
- A 4WIS hybrid A* algorithm is developed that explicitly embeds Ackermann steering, diagonal movement, and zero-turn rotation modes, and incorporates these motion modes into the node expansion process through kinematically feasible motion primitives. Node cost and mode

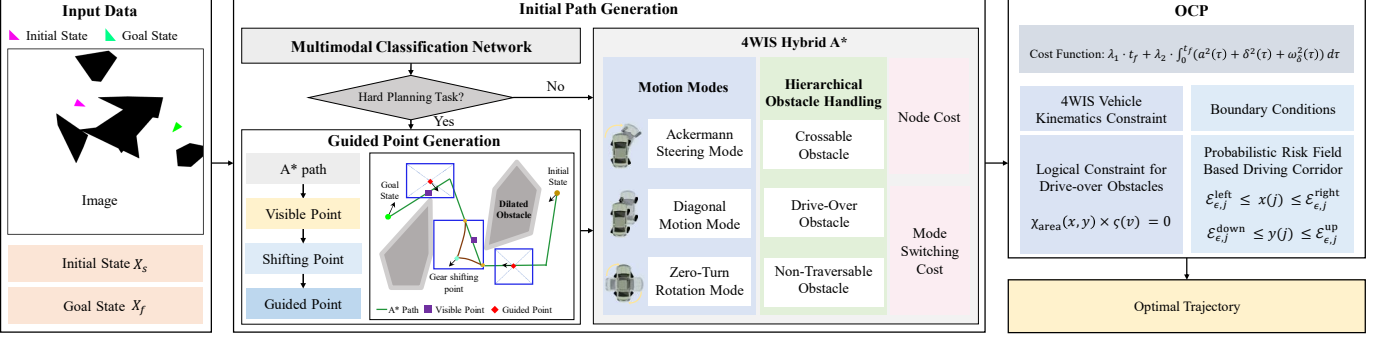


Fig. 2. Overview of the framework. We use image and vehicle state as inputs, and employ a multimodal classification network to assess the complexity of the planning task. For hard tasks, a guided point generation strategy is activated to facilitate the 4WIS hybrid A* path planning, which accommodates multiple motion modes and incorporates hierarchical obstacle handling strategies. The hybrid A* initial path is a warm start for solving the OCP.

switching cost are also designed to reduce unnecessary reversals and frequent mode switches.

- We introduce a hierarchical obstacle handling strategy into the 4WIS hybrid A* framework, which enables efficient and explainable planning in obstacle-dense environments. This strategy prioritizes crossing when feasible, and otherwise selects to drive over or avoid obstacles.
- A probabilistic risk field-based driving corridor method is proposed that accounts for the motion uncertainty of dynamic obstacles and formulates linear collision avoidance constraints to reduce complexity. In addition, logical constraints for “drive-over” obstacles are incorporated to ensure safety by limiting the vehicle’s velocity, ensuring interpretable optimization decisions.

B. Related Works

1) **Motion Planning:** Search-based methods explore the state space using heuristic algorithms to generate feasible trajectories. [9] proposed an A*-based planner with enhanced node expansion strategies. [10] presented the hybrid A* algorithm, which integrates discrete search with continuous space. [11] proposed a fault-tolerant hybrid A* (FTHA) algorithm that ensures completeness by falling back to A*, but the path may violate kinematic constraints. [12] proposed guide points to increase search efficiency. Optimization-based methods formulate trajectory planning as an optimization problem, using numerical techniques to generate a feasible trajectory. [13] proposed a trajectory planning method for 2.5D environments. [14] developed a Successive Linearization in Feasible Set algorithm that linearizes collision constraints. [15] formulated the trajectory planning task as a mixed-integer nonlinear programming problem.

Different from existing studies, we propose a multimodal classification network-guided trajectory planning framework that determines the necessity of guided points. A guided points generation strategy is designed to decompose the complex planning task into local subtasks, improving planning efficiency in cluttered environments.

2) **4WIS Vehicle Motion Planning:** Most existing motion planning studies are developed for conventional front-wheel drive vehicles, with limited attention given to 4WIS systems. [16] proposed an improved A* algorithm for differential wheeled vehicles. [17] developed a shape-aware lifelong

planning A* algorithm for differential wheeled robots. [18] incorporated a 4WIS motion modes decision-making mechanism into the A* framework. [19] presented a B-spline-based trajectory planning method for smooth steering mode switching in 4WIS vehicles. [20] presented a kinematics-based trajectory planning algorithm for 4WIS vehicles, focusing on steering and velocity planning. [21] proposed a steer-by-wire control approach for 4WIS vehicles that operates without trajectory planning. [22] presented a clothoid-based trajectory planning method for 4WIS-4WID vehicles.

Different from existing studies, we develop a 4WIS hybrid A* algorithm that explicitly incorporates Ackermann steering mode, diagonal movement mode, and zero-turn rotation mode to generate an initial path that satisfies vehicle kinematics.

3) **Obstacle Handling Strategy:** Handling obstacles requires a balance between the solution quality and computational efficiency. Static obstacles are among the most prevalent obstacles in environments. [23] used a Voronoi-based roadmap and tunnel constraints to handle non-traversable obstacles. [13] proposed a trajectory planning framework for “drive-over” obstacles like road shoulders and slopes. [24] focuses on local logical constraints for “drive-over” obstacles, such as speed bumps. [25] proposed a double-layer collision checking method for “crossable” obstacles. To handle dynamic obstacles, [26] modeled obstacle motion and position uncertainties using Gaussian distributions. [27] enhanced reachable set generation by integrating collision probabilities. [28] used a Linear Quadratic Gaussian framework to enhance robustness under prediction uncertainty. [29] modeled risks for static and dynamic obstacles, while [30] extended it with a time-series motion risk field for spatiotemporal mapping.

Different from existing studies, we integrate a hierarchical obstacle handling strategy into the 4WIS hybrid A* framework, selecting expansion directions based on obstacle attributes. For dynamic obstacles, we propose a probabilistic risk field-based corridor method that accounts for motion uncertainty. Logical constraints for “drive-over” obstacles are also introduced to limit vehicle velocity to enhance stability.

II. OVERALL FRAMEWORK

Trajectory planning is formulated as an OCP, and we propose a 4WIS hybrid A* algorithm for generating the initial path, serving as a warm start for the trajectory optimization.

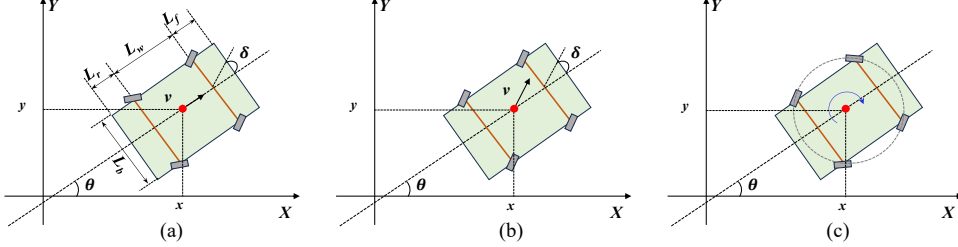


Fig. 3. Schematics of 4WIS vehicle motion modes. (a) Ackermann steering mode; (b) Diagonal movement mode; (c) Zero-turn rotation mode.

A. Vehicle Kinematic Model

Three motion modes of the 4WIS vehicle, including Ackermann steering mode, diagonal movement mode, and zero-turn rotation mode, are incorporated into the planning framework.

1) **Ackermann steering mode:** The 4WIS vehicle performs curvilinear motion while satisfying Ackermann steering geometry constraints, as shown in Fig. 3(a). The kinematic model can be described:

$$\begin{bmatrix} \dot{x}(t) \\ \dot{y}(t) \\ \dot{v}(t) \\ \dot{\theta}(t) \\ \dot{\delta}(t) \end{bmatrix} = \begin{bmatrix} v(t) \cdot \cos \theta(t) \\ v(t) \cdot \sin \theta(t) \\ v(t) \\ 2v(t) \cdot \tan \delta(t)/L_w \\ \omega_\delta(t) \end{bmatrix}, t \in [0, t_f], \quad (1)$$

where $x(t)$ and $y(t)$ denote the longitudinal and lateral coordinates of the vehicle center point, respectively, and $v(t)$ is the velocity, $\theta(t)$ is the heading angle, $\delta(t)$ is the front-wheel steering angle. $a(t)$ is the acceleration, L_w is the vehicle wheelbase, $\omega_\delta(t)$ is the front wheel angular velocity, t_f is the planning duration.

2) **Diagonal movement mode:** All wheels steer at the same angle $\delta(t)$, while the vehicle's orientation $\theta(t)$ remains constant, enabling motion along the direction $(\theta(t) + \delta(t))$, as shown in Fig. 3(b). The kinematic model can be described:

$$\begin{bmatrix} \dot{x}(t) \\ \dot{y}(t) \\ \dot{v}(t) \\ \dot{\theta}(t) \\ \dot{\delta}(t) \end{bmatrix} = \begin{bmatrix} v(t) \cdot \cos(\theta(t) + \delta(t)) \\ v(t) \cdot \sin(\theta(t) + \delta(t)) \\ v(t) \\ 0 \\ 0 \end{bmatrix}, t \in [0, t_f]. \quad (2)$$

3) **Zero-turn rotation mode:** The vehicle steers around the center point, and the orientation angle θ is changing, as shown in Fig. 3(c). The kinematic model can be described:

$$\begin{bmatrix} \dot{x}(t) \\ \dot{y}(t) \\ \dot{v}(t) \\ \dot{\theta}(t) \\ \dot{\delta}(t) \end{bmatrix} = \begin{bmatrix} 0 \\ 0 \\ 0 \\ \omega_\theta \\ 0 \end{bmatrix}, t \in [0, t_f], \quad (3)$$

where ω_θ is the yaw rate, assumed to be constant in this study.

B. Optimal Control Problem

1) **Cost Function:** Trajectory planning is formulated as an OCP, with a cost function that considers the planning efficiency, driving comfort, and smoothness:

$$J_c = \lambda_1 \cdot t_f + \lambda_2 \cdot \int_0^{t_f} (a^2(\tau) + \delta^2(\tau) + w_\delta^2(\tau)) \cdot d\tau, \quad (4)$$

where λ_1 and λ_2 are weighting coefficients.

2) **Collision Avoidance Constraint:** Referring to [11], the driving corridor approach is used to linearize the non-differentiable and non-convex collision avoidance constraints and improve computational efficiency. [11] uses a fixed step size, and a large step size may lead to suboptimal solutions, while a small step size increases computational cost. To address this, an adaptive step size strategy is designed to generate the driving corridor. As illustrated in Fig. 4, the expansion starts from the sampling point (yellow dot) and progressively enlarges the driving corridor with a varying step size. The expansion is performed in four directions: upward, rightward, downward, and leftward, and the step size is dynamically adjusted based on the outcomes of each expansion. After each expansion in a given direction, the step size for the next expansion is updated. A successful expansion indicates that a sufficient space remains, while a failed expansion indicates a collision with the obstacle (see Fig. 4). The number of failed expansions is recorded, and once it reaches a predefined threshold in a given direction, expansion along that direction is terminated.

Let $(x(j), y(j))$ be the current sampling point, and the expansion distance l_j^R in each direction R is used to represent the driving corridor \mathcal{C}_j :

$$\begin{cases} \mathcal{C}_j = \{(x, y) \mid \mathcal{E}_j^{\text{left}} \leq x \leq \mathcal{E}_j^{\text{right}}, \mathcal{E}_j^{\text{down}} \leq y \leq \mathcal{E}_j^{\text{up}}\}, \\ \mathcal{E}_j^{\text{up}} = y(j) + l_j^{\text{up}}, \mathcal{E}_j^{\text{down}} = y(j) - l_j^{\text{down}}, \\ \mathcal{E}_j^{\text{right}} = x(j) + l_j^{\text{right}}, \mathcal{E}_j^{\text{left}} = x(j) - l_j^{\text{left}}, \end{cases} \quad (5)$$

where $R \in \{\text{upward, rightward, downward, leftward}\}$. $\mathcal{E}_j^{\text{up}}$, $\mathcal{E}_j^{\text{right}}$, $\mathcal{E}_j^{\text{down}}$, and $\mathcal{E}_j^{\text{left}}$ denote the boundaries of the driving corridor in each direction.

3) **Boundary Conditions:** It defines the initial state constraint and the terminal constraint. The trajectory is discretized as $\{s(0), s(1), \dots, s(N_f)\}$, $N_f = t_f/\Delta t$, Δt is the sampling time interval. The initial state $s(0)$ and the terminal state constraints $s(N_f)$ are described as

$$s(0) = s_{t_0}, \quad s(N_f) = s_{t_f}, \quad (6)$$

where s_{t_0} and s_{t_f} represent the initial and goal state variables.

4) **Optimization Model:** The trajectory planning problem can be written as the following OCP:

$$\begin{aligned} \min \quad & J_c \\ \text{s.t.} \quad & \text{Vehicle Kinematic Constraints: (1), (2), (3),} \\ & \text{Collision Avoidance Constraints: (5),} \\ & \text{Boundary Conditions Constraints: (6),} \end{aligned} \quad (7)$$

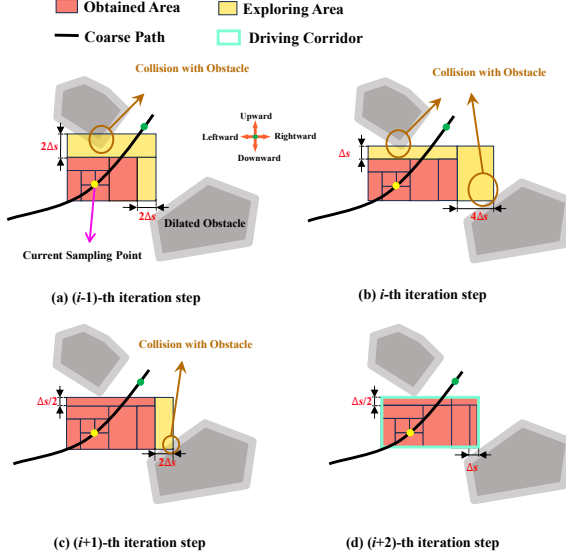


Fig. 4. Adaptive step size strategy for driving corridor generation. In the $(i-1)$ th iteration step, the step size is $2\Delta s$ in the rightward and upward direction. A collision encountered in the upward direction triggers a reduction in step size, which continues until a collision-free expansion is achieved. Conversely, in the rightward direction, the step size increases iteratively until a collision is detected, after which it is reduced to enable further exploration. The generated driving corridor is shown in (d) after successful expansion.

where the cost function is J_c , and vehicle kinematic constraints, boundary condition constraints, and collision avoidance constraints are included.

III. GUIDED POINTS GENERATION STRATEGY

A. Visible Points

We employ the A* algorithm to generate a feasible path from the initial state to the goal state. Let $P = \{p_i\}_{i=1}^N$ be the waypoints along this path, and $p_i = (p_{i,x}, p_{i,y})$ denote a discrete waypoint, N is the number of points. The A* path implicitly contains environmental information, such as obstacle locations and available free space. To set the guided points, we define the visible points (see Fig. 5(a)) as follows.

Visible Points. Consider an environment with obstacle space $O_{\text{obs}} \subseteq \mathbb{R}^2$ and a free space $O_{\text{free}} \subseteq \mathbb{R}^2$. Let $p_A \in O_{\text{free}}$ and $p_B \in O_{\text{free}}$ be two points in the free space. The line segment connecting p_A and p_B is defined as $l_{A,B} = \{(1-\lambda)p_A + \lambda p_B \mid 0 \leq \lambda \leq 1\}$. If $l_{A,B} \cap O_{\text{obs}} = \emptyset$, then the point p_B is defined as a visible point of p_A . All visible points of a point p_A are stored in $P_A^{\text{vis}} = \{p_i\}_{i=1}^{N_v}$, N_v is the number of visible points for the point p_A .

Farthest Visible Point. If $\exists p_f \in P_A^{\text{vis}}, \forall p_j \in P_A^{\text{vis}} (j \neq f)$, it holds $\|l_{p_A, p_f}\| \geq \|l_{p_A, p_j}\|$, then the point p_f is defined as the farthest visible point of a point p_A . We denote the farthest visible point as $p_f = \mathcal{F}(p_A)$, \mathcal{F} is the mapping function. The k -th recursive operation of this mapping is denoted as $\mathcal{F}^k(p_A)$, and satisfies:

$$\mathcal{F}^0(p_A) \triangleq p_A, \quad \mathcal{F}^{k+1}(p_A) \triangleq \mathcal{F}(\mathcal{F}^k(p_A)).$$

Consecutive Farthest Visible Point Set. The consecutive farthest visible point set from p_1 to p_N is denoted as $V_{p_1} = \{p_1, \mathcal{F}_P^1(p_1), \dots, \mathcal{F}^m(p_1)\}$, $m \in \mathbb{Z}$, $1 \leq m \leq N$, $\mathcal{F}^m(p_1) =$

p_N , $|V_{p_1}| = m + 1$. The process of generating the consecutive farthest visible point set V_{p_1} along the A* path is detailed in Algorithm A.1 (see Appendix).

B. Gear Shifting Points

The gear shifting point is essential in setting the guided points. We first evaluate whether gear shifting is required and then identify the region along the A* path that finds the largest free space to set the gear shifting point. As shown in Fig. 6, α_1 and α_2 are defined as the angles between the vehicle's initial and goal orientations and the A* path, respectively. If $\cos \alpha_1 \cos \alpha_2 > 0$, we assume that the vehicle can proceed directly without gear shifting, as illustrated in Fig. 6(a). In contrast, if $\cos \alpha_1 \cos \alpha_2 \leq 0$, we assume that the gear shifting is required, as illustrated in Fig. 6(b).

We determine the appropriate shifting point only when gear shifting is required. Starting from the consecutive farthest visible point V_{p_1} , we expand outward in all directions at each point in V_{p_1} —similar to constructing a driving corridor—to form a series of local rectangular regions along the A* path. These local rectangles are denoted as $\mathcal{D} = \{\mathcal{D}_{p_1}, \mathcal{D}_{p_2}, \dots, \mathcal{D}_{p_N}\}$. To improve the feasibility of gear shifting, the largest rectangle among them is selected for determining the gear shifting point, as illustrated in Fig. 5(b). The intersection points between this largest rectangle and the A* path are denoted as p_{I_1} and p_{I_2} . To ensure smooth transition and trajectory continuity, two clothoid curves are constructed based on p_{I_1} and p_{I_2} , respectively. The gear shifting point p_g is defined as the intersection of these two clothoid curves, which can be obtained by solving the following equations:

$$\mathcal{C}(\theta_{p_{I_1}}, R_{\min}, l_{\text{curve}}) = \mathcal{C}(\theta_{p_{I_2}}, R_{\min}, l_{\text{curve}}), \quad (8)$$

where $\mathcal{C}(\cdot)$ denotes the clothoid curve parameterized by the heading angle, minimum turning radius R_{\min} , and curve length l_{curve} . $\theta_{p_{I_1}}$ and $\theta_{p_{I_2}}$ are the heading angles of the two points p_{I_1} and p_{I_2} , respectively.

C. Generation of Guided Points

The gear shifting point p_g is a special guided point when gear shifting is needed. In addition, the guided points are selected at the center of each rectangle in $\mathcal{D} = \{\mathcal{D}_{p_1}, \mathcal{D}_{p_2}, \dots, \mathcal{D}_{p_N}\}$. We use $(g_{i,x}, g_{i,y})$ to denote the position of the guided point g_i . Moreover, each guided point g_i is assigned an orientation angle θ_{g_i} based on the angles α_1 and α_2 . Four cases are considered:

Case 1: $\cos \alpha_1 > 0, \cos \alpha_2 > 0$. The vehicle can reach the goal by moving *forward* without gear shifting:

$$\theta_{g_i} = \text{atan2}(g_{i+1,y} - g_{i,y}, g_{i+1,x} - g_{i,x}) \quad (9)$$

Case 2: $\cos \alpha_1 < 0, \cos \alpha_2 < 0$. The vehicle can *reverse* to the goal without gear shifting:

$$\theta_{g_i} = \text{atan2}(g_{i,y} - g_{i+1,y}, g_{i,x} - g_{i+1,x}) \quad (10)$$

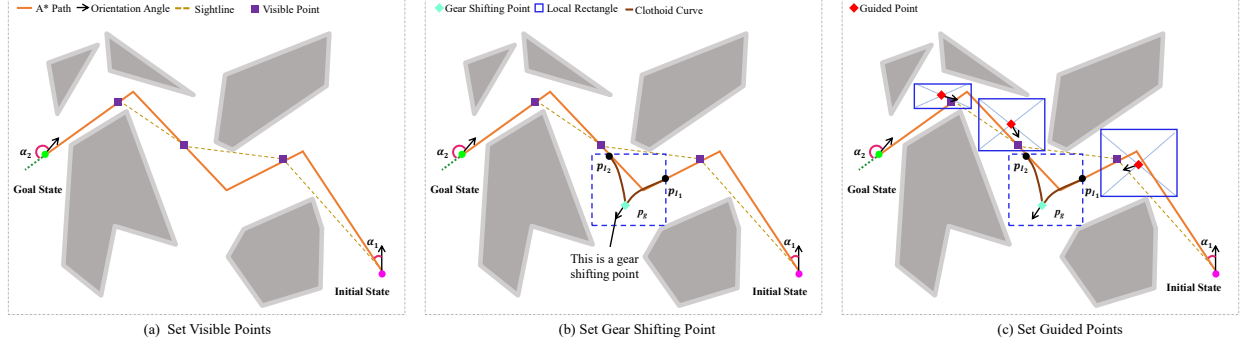


Fig. 5. Guided points setting. (a) Visible points. (b) Gear shifting points. The intersection points between the local rectangle and the A* path are denoted as p_{I_1} and p_{I_2} . Two clothoid curves are generated based on p_{I_1} and p_{I_2} , and the gear shifting point p_g is defined as their intersection. (c) Guided points. The center of each rectangle expanded from a visible point is designated as a guided point. Gear shifting points are treated as special cases of guided points.

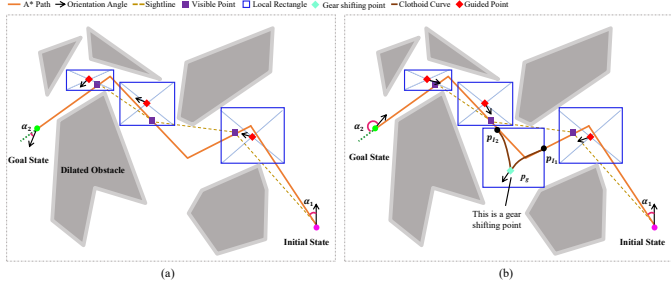


Fig. 6. Necessity of gear shifting point. (a) $\cos \alpha_1 \cdot \cos \alpha_2 > 0$. Gear shifting is unnecessary. (b) $\cos \alpha_1 \cdot \cos \alpha_2 \leq 0$. Gear shifting is required.

Case 3: $\cos \alpha_1 \geq 0, \cos \alpha_2 \leq 0$. Gear shifting is required. The vehicle moves *forward* between the initial state X_s and p_g , and *reverses* between p_g and the goal state X_f :

$$\theta_{g_i} = \begin{cases} \text{atan2}(g_{i+1,y} - g_{i,y}, g_{i+1,x} - g_{i,x}), & \text{if } g_i \in [X_s, p_g], \\ \text{atan2}(g_{i,y} - g_{i+1,y}, g_{i,x} - g_{i+1,x}), & \text{otherwise.} \end{cases} \quad (11)$$

Case 4: $\cos \alpha_1 < 0, \cos \alpha_2 > 0$. Gear shifting is required. The vehicle *reverses* between X_s and p_g , and moves *forward* between p_g and X_f :

$$\theta_{g_i} = \begin{cases} \text{atan2}(g_{i,y} - g_{i+1,y}, g_{i,x} - g_{i+1,x}), & \text{if } g_i \in [X_s, p_g], \\ \text{atan2}(g_{i+1,y} - g_{i,y}, g_{i+1,x} - g_{i,x}), & \text{otherwise.} \end{cases} \quad (12)$$

The guided points g_i are represented as $(g_{i,x}, g_{i,y}, \theta_{g_i})$, which are used to instruct the hybrid A* algorithm by decomposing the complex planning task into local subtasks.

IV. MULTIMODAL CLASSIFICATION NETWORK

As discussed previously in Section III, we propose a guided point generation strategy, aiming to enhance the search efficiency of hybrid A* in our framework. However, applying this guided point strategy to simple tasks that have high search efficiency may incur unnecessary computational overhead. To improve overall computational efficiency, we introduce a multimodal classification network to assess scenario complexity. The guided point generation strategy is activated only when the scenario is classified as a hard planning task.

A. Model Architecture

1) *Data Preprocessing*: Our model takes the scenario image and the vehicle states as input, and outputs the classi-

fication result, *i.e.*, hard/easy planning task, as illustrated in Fig. 7. Scenario images are generated through simulation, with distinct colors used to annotate key elements such as the initial state, goal state, obstacles, and free space (see Fig. 7). The vehicle state data includes the initial and goal state (position and heading) of the vehicle, represented as $X_s = (x_s, y_s, \theta_s)$ and $X_f = (x_f, y_f, \theta_f)$, respectively.

Initial Mask, Goal Mask, and Obstacle Mask. To capture the spatial distribution of the initial state, the goal state, and obstacles in the image, we define the initial mask indicator function $\mathbb{1}_{\text{init}}(i, j)$, the goal mask indicator function $\mathbb{1}_{\text{goal}}(i, j)$, and the obstacle mask indicator function $\mathbb{1}_{\text{obs}}(i, j)$ based on the color of the pixel:

$$\mathbb{1}_{\text{init}}(i, j) = \begin{cases} 1, & \text{if } P(i, j) = (255, 0, 255), \\ 0, & \text{otherwise.} \end{cases} \quad (13)$$

$$\mathbb{1}_{\text{goal}}(i, j) = \begin{cases} 1, & \text{if } P(i, j) = (0, 255, 0), \\ 0, & \text{otherwise.} \end{cases} \quad (14)$$

$$\mathbb{1}_{\text{obs}}(i, j) = \begin{cases} 1, & \text{if } P(i, j) = (0, 0, 0), \\ 0, & \text{otherwise,} \end{cases} \quad (15)$$

where $P(i, j)$ is the pixel value. $P(i, j) = (255, 0, 255)$ indicates that the pixel is magenta, which is the initial state; $P(i, j) = (0, 255, 0)$ indicates that the pixel is green, which is the goal state; $P(i, j) = (0, 0, 0)$ indicates that the pixel is black, which is the obstacle. Next, we compute the number of pixels located in the initial state, the goal state, and the obstacle areas in the image:

$$N_{\mathcal{M}} = \sum_{i=1}^W \sum_{j=1}^H \mathbb{1}_{\mathcal{M}}(i, j), \quad \mathcal{M} \in \{\text{init, goal, obs}\}, \quad (16)$$

where $N_{\mathcal{M}}$ represents the total number of pixels within the region \mathcal{M} , where $\mathcal{M} \in \{\text{init, goal, obs}\}$ corresponds to the initial state, goal state, and obstacle area, respectively. H and W are the height and width of the image, respectively. The total number of pixels in the scenario image $N_{\text{total}} = W \times H$ is also computed. The proportions of the initial state region, goal state region, and obstacle region in the entire image are

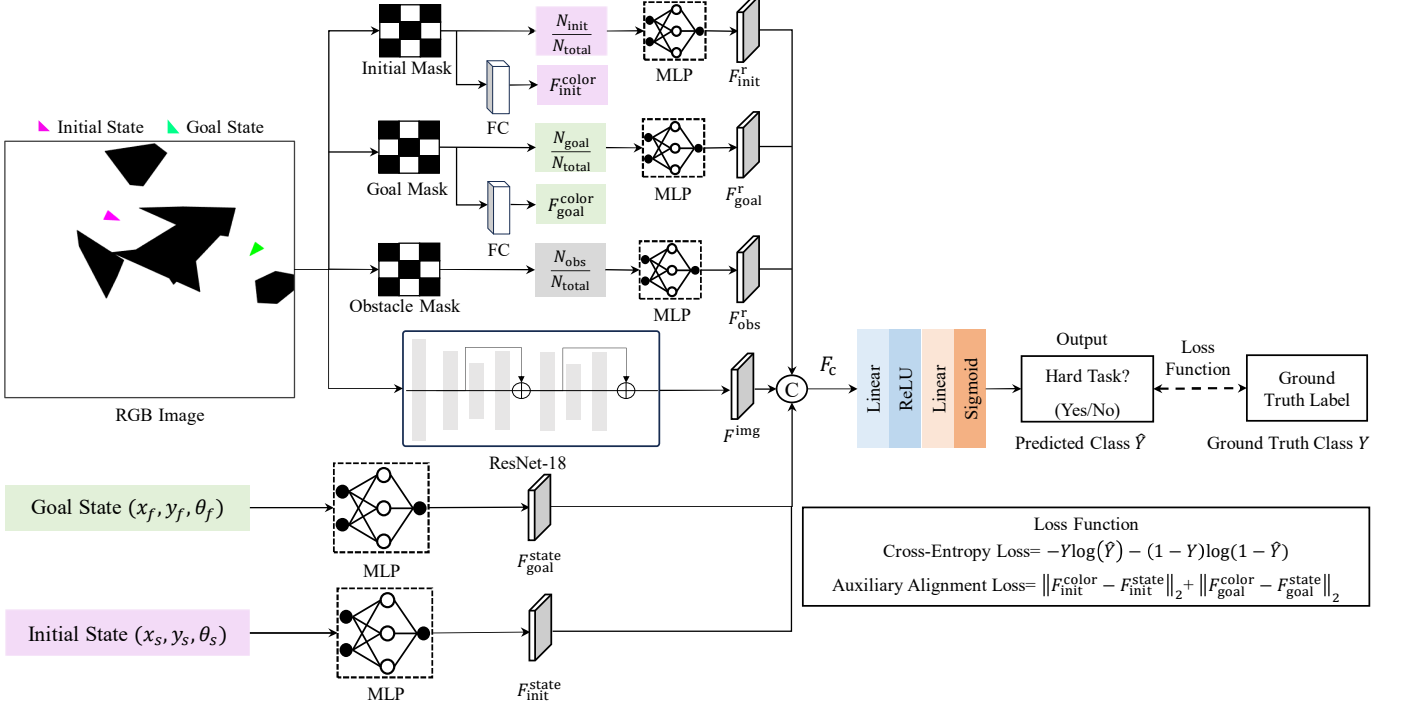


Fig. 7. Overview of the multimodal classification network. Semantic masks for the initial region, goal region, and obstacles are generated from the RGB image to capture spatial distributions. A ResNet-18 extracts visual features F^{img} , while multiple MLPs encode the vehicle’s initial and goal states $F^{\text{state}}_{\text{init}}$, $F^{\text{state}}_{\text{goal}}$ and region-based color features $F^{\text{color}}_{\text{init}}$, $F^{\text{color}}_{\text{goal}}$, $F^{\text{color}}_{\text{obs}}$. Here, $N_{\text{init}}/N_{\text{total}}$, $N_{\text{goal}}/N_{\text{total}}$, $N_{\text{obs}}/N_{\text{total}}$ represent the proportion of pixels belonging to the initial, goal, and obstacle regions, respectively. All features are concatenated into a combined vector F_c , which is passed through fully connected layers to classify whether the planning task is considered hard. An auxiliary alignment loss encourages consistency between the color-derived and state-derived features, enhancing the alignment across modalities.

represented by $\frac{N_{\text{init}}}{N_{\text{total}}}$, $\frac{N_{\text{goal}}}{N_{\text{total}}}$, and $\frac{N_{\text{obs}}}{N_{\text{total}}}$, respectively. Simultaneously, these proportions are processed with an MLP separately to extract feature representations:

$$F_{\mathcal{M}}^r = \text{MLP} \left(\frac{N_{\mathcal{M}}}{N_{\text{total}}} \right), \quad \mathcal{M} \in \{\text{init, goal, obs}\}, \quad (17)$$

where each $F_{\mathcal{M}}^r$ is an extracted ratio feature representation.

Image Feature Extraction. Simultaneously, the raw RGB image is passed through a pre-trained ResNet-18 backbone to extract deep visual features F^{img} [31]. The input image is denoted as $I \in \mathbb{R}^{H \times W \times 3}$ and the image feature representation F^{img} is written as

$$F^{\text{img}} = \text{ResNet18}(I). \quad (18)$$

Vehicle State Feature Extraction. Simultaneously, the initial state X_s and goal state X_f are processed with MLP separately to extract individual feature representations:

$$F^{\text{state}}_{\text{init}} = \text{MLP}(X_s), \quad F^{\text{state}}_{\text{goal}} = \text{MLP}(X_f), \quad (19)$$

where $F^{\text{state}}_{\text{init}}$ and $F^{\text{state}}_{\text{goal}}$ are feature vectors extracted from the initial and goal states, respectively.

Multi-modal Feature Fusion. The image features F^{img} , initial state features $F^{\text{state}}_{\text{init}}$, goal state features $F^{\text{state}}_{\text{goal}}$, initial state ratio features F^r_{init} , goal state ratio features F^r_{goal} and obstacle ratio features F^r_{obs} are concatenated together to form a combined feature vector F_c :

$$F_c = \text{Concat}(F^{\text{img}}, F^{\text{state}}_{\text{init}}, F^{\text{state}}_{\text{goal}}, F^r_{\text{init}}, F^r_{\text{goal}}, F^r_{\text{obs}}) \quad (20)$$

Here, F_c is subsequently passed through two fully connected (Linear) layers with a ReLU activation in between, followed by a Sigmoid output layer producing \hat{Y} , which classifies whether the task at hand is a “Hard Task” (Yes/No).

$$\hat{Y} = \text{MLP}(F_c), \quad (21)$$

where \hat{Y} is the probability of the hard planning task. It is classified as a hard planning task if the probability of the hard task is larger than 0.5.

B. Loss Function

We combine the standard binary cross-entropy loss with an alignment loss to ensure both classification accuracy and meaningful spatial embeddings.

1) **Cross-entropy Loss:** The binary cross-entropy loss \mathcal{L}_{CE} is used for the primary binary classification task:

$$\mathcal{L}_{\text{CE}} = -Y \log(\hat{Y}) - (1 - Y) \log(1 - \hat{Y}), \quad (22)$$

where Y represents the ground truth label.

2) **Auxiliary Alignment Loss:** The alignment loss is defined to align the color features and state features of the initial and goal state regions in the scenario image. We first compute the average pixel values of the initial state and goal state regions:

$$c_{\text{init}} = \frac{\sum_{i=1}^W \sum_{j=1}^H \mathbb{1}_{\text{init}}(i, j) \cdot P(i, j)}{N_{\text{init}}}, \quad (23)$$

$$c_{\text{goal}} = \frac{\sum_{i=1}^W \sum_{j=1}^H \mathbb{1}_{\text{goal}}(i, j) \cdot P(i, j)}{N_{\text{goal}}}, \quad (24)$$

where c_{init} and c_{goal} are the average pixel values of the initial state and goal state region, respectively. c_{init} and c_{goal} are passed through separate fully connected layers to obtain feature embeddings:

$$F_{\text{init}}^{\text{color}} = \text{FC}(c_{\text{init}}), F_{\text{goal}}^{\text{color}} = \text{FC}(c_{\text{goal}}), \quad (25)$$

where $F_{\text{init}}^{\text{color}}$ and $F_{\text{goal}}^{\text{color}}$ represent the feature embeddings of the initial and goal state regions, respectively. $\text{FC}(\cdot)$ is a fully connected layer. To encourage the spatial consistency between the color and state representations, we introduce an auxiliary alignment loss $\mathcal{L}_{\text{align}}$:

$$\mathcal{L}_{\text{align}} = \|F_{\text{init}}^{\text{color}} - F_{\text{init}}^{\text{state}}\|_2 + \|F_{\text{goal}}^{\text{color}} - F_{\text{goal}}^{\text{state}}\|_2. \quad (26)$$

The auxiliary alignment loss $\mathcal{L}_{\text{align}}$ is defined to minimize the mean squared errors between the color features and state features of both the initial and goal state regions.

The total loss function $\mathcal{L}_{\text{total}}$ is defined as the weighted sum of the cross-entropy loss \mathcal{L}_{CE} and the alignment loss $\mathcal{L}_{\text{align}}$:

$$\mathcal{L}_{\text{total}} = \lambda_{\text{CE}} \mathcal{L}_{\text{CE}} + \lambda_{\text{align}} \mathcal{L}_{\text{align}}, \quad (27)$$

where λ_{CE} and λ_{align} are hyperparameters. With the aid of the multimodal classification network, our method can adaptively determine whether to utilize guided points based on task complexities. For planning tasks classified as “easy”, guided points are omitted to avoid unnecessary computational overhead. In contrast, for tasks identified as “hard”, guided points are employed to enhance the efficiency and success rate of the 4WIS hybrid A* algorithm. Overall, this multimodal classification network is supposed to save computation time for “easy” cases and improve the planning efficiency and success rate for “hard” cases.

V. 4WIS HYBRID A* FRAMEWORK

This section introduces a 4WIS hybrid A* algorithm that includes three motion modes during node expansion. We set node-cost and mode-switch penalties to reduce unnecessary reversing and frequent switching. Besides, we employ the obstacle attributes to determine the expansion direction to improve path efficiency. Finally, the enhanced 4WIS hybrid A* that integrates with the guided points and obstacle handling strategies is described.

A. Heuristic Design

During node expansion of 4WIS hybrid A*, the parent node is represented as $n_p = (x_p, y_p, \theta_p, v_p, \delta_p)$ and the child node is $n_c = (x_c, y_c, \theta_c, v_c, \delta_c)$. The motion mode of n_c is $M(n_c)$. $M(n_c) = 1$ represents the Ackermann steering mode, $M(n_c) = 2$ represents diagonal movement mode, and $M(n_c) = 3$ represents zero-turn rotation mode. To ensure smooth mode transitions, each child node is evaluated by a comprehensive cost $F(n_c)$:

$$F(n_c) = \begin{cases} G(n_c) + H(n_c), & \text{if } M(n_p) = M(n_c), \\ G(n_c) + I(n_c) + H(n_c), & \text{otherwise,} \end{cases} \quad (28)$$



Fig. 8. Schematic diagrams of three types of obstacles. (a) Traffic cones, representing “non-traversable” obstacles that must be avoided; (b) Stones in the middle of the road, representing “crossable” obstacles that can be carefully navigated across but not directly driven over; (c) A cardboard box on the road, representing “drive-over” obstacles that can be navigated with low speeds.

where $G(n_c)$ denotes the node cost function, $I(n_c)$ is the mode switching cost, and $H(n_c)$ is the heuristic cost. If the motion mode of the parent node and the child node is the same, $F(n_c)$ is defined as the sum of $G(n_c)$ and $H(n_c)$. When $M(n_p) \neq M(n_c)$, $F(n_c)$ is the sum of $G(n_c)$, $I(n_c)$, and $H(n_c)$. $H(n_c)$ is the standard heuristic cost in hybrid A* [10]. The node cost $G(n_c)$ and the mode switching cost $I(n_c)$ are shown below.

1) *Node Cost Function*: Different node costs are designed for each child node generated by the three node expansion methods, and the node cost $G(n_c)$ is described as

$$G(n_c) = \begin{cases} |v_p - v_c| w_{r,a} + |\delta_p - \delta_c| w_{t,a}, & M(n_c) = 1, \\ |v_p - v_c| w_{r,d} + |\delta_p - \delta_c| w_{t,d}, & M(n_c) = 2, \\ |\theta_p - \theta_c| w_{o,z}, & M(n_c) = 3, \end{cases} \quad (29)$$

where $w_{r,a}$ and $w_{t,a}$ are the reversing and steering change penalties for Ackermann steering, respectively; $w_{r,d}$ and $w_{t,d}$ are the reversing and steering change penalties for diagonal movement; $w_{o,z}$ is the orientation change penalty for the zero-turn rotation mode.

2) *Mode Switching Cost Function*: While 4WIS vehicles provide flexible maneuverability through multiple motion modes, frequent switching should be penalized. The mode switching cost is defined as

$$I(n_c) = I_{\text{recover}} + I_{\text{change}}, \quad (30)$$

where I_{recover} penalizes resetting the current wheel angle, and I_{change} penalizes entering the next motion mode:

$$I_{\text{recover}} = \begin{cases} w_{r,1} \cdot \delta_p, & M(n_p) = 1, \\ w_{r,2} \cdot \delta_p, & M(n_p) = 2, \\ w_{r,3}, & M(n_p) = 3, \end{cases} \quad (31)$$

$$I_{\text{change}} = \begin{cases} w_{r,1} \cdot \delta_c, & M(n_c) = 1, \\ w_{r,2} \cdot \delta_c, & M(n_c) = 2, \\ w_{r,3} \cdot |\theta_p - \theta_c|, & M(n_c) = 3, \end{cases} \quad (32)$$

where $w_{r,1}$, $w_{r,2}$, and $w_{r,3}$ are the penalty coefficients corresponding to Ackermann steering, diagonal movement, and zero-turn rotation, respectively.

B. Static Obstacle Handling Strategies

To enhance the planning efficiency of the 4WIS hybrid A* in constrained environments, this study categorizes the static obstacles into “non-traversable”, “crossable”, or “drive-over” obstacles, and sets different node expansion methods for different static obstacles in 4WIS hybrid A*.

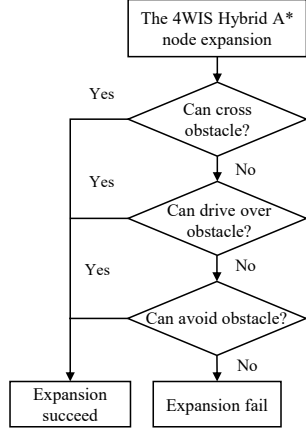


Fig. 9. Hierarchical obstacle handling strategy in the 4WIS hybrid A* node expansion. The strategy first prioritizes crossing the obstacle when feasible; if crossing is impossible, it then attempts to drive over the obstacle. If neither crossing nor driving over is feasible, the strategy resorts to avoidance. If all these options fail, the node expansion fails.

1) *Obstacle Type*: The static obstacles are categorized into three types based on their impacts on the safety of trajectory planning tasks: **Non-traversable obstacles**, such as pedestrians, vehicles, and traffic cones (see Fig. 8 (a)), which pose significant collision risks and must be strictly avoided during path planning; **Crossable obstacles**, such as small rocks or shallow potholes located centrally on the roadway (see Fig. 8 (b)), can be safely traversed if it does not collide with vehicle wheels and chassis; **Drive-over obstacles**, such as puddles, speed bumps, and cardboard boxes on the road (see Fig. 8 (c)), can be driven over at low speeds without compromising vehicle safety.

The “Non-traversable” and “drive-over” obstacles can be readily identified. However, determining “crossable” obstacles is a non-trivial task, as it necessitates evaluating potential collisions with the vehicle’s wheels or chassis. This involves expanding trajectories using the vehicle’s kinematic models, such as (1), (2), and (3), during the node expansion phase of the 4WIS hybrid A* algorithm, which results in an expanded trajectory set T . For each trajectory $T_j \in T$ and the obstacle O_i , a collision check is performed to determine the feasibility of the path.

First, to assess whether an obstacle collides with the vehicle’s chassis, we define a height-based evaluation function $f_{\text{height}}(h_{O_i}, h_v)$ that compares the obstacle’s height with the vehicle’s chassis clearance height:

$$f_{\text{height}}(h_{O_i}, h_v) = \begin{cases} 1, & \text{if } h_{O_i} < h_v, \\ 0, & \text{if } h_{O_i} \geq h_v, \end{cases} \quad (33)$$

where h_{O_i} is the height of obstacle O_i and h_v is the vehicle’s ground clearance, $f_{\text{height}}(h_{O_i}, h_v)$ is a binary variable, in which “0” indicates unsafe, and “1” indicates safe.

Next, to assess whether the obstacle can be crossed without wheel contacts, we define $f_{\text{wheel}}(T_j, O_i)$ as follows:

$$f_{\text{wheel}}(T_j, O_i) = \begin{cases} 1, & \text{if } \text{proj}(\mathbf{w}(T_j)) \cap \text{proj}(O_i) = \emptyset, \\ 0, & \text{if } \text{proj}(\mathbf{w}(T_j)) \cap \text{proj}(O_i) \neq \emptyset, \end{cases} \quad (34)$$

where $f_{\text{wheel}}(T_j, O_i)$ is also a binary variable, in which “0” indicates unsafe, and “1” indicates safe. $\mathbf{w}(T_j)$ is the global position of the vehicle’s wheels along the trajectory T_j . The operator $\text{proj}(\cdot)$ denotes the projection onto the (x, y) plane. $\text{proj}(\mathbf{w}(T_j))$ is the projected wheel positions and $\text{proj}(O_i)$ is the projection of the obstacle O_i . If $\text{proj}(\mathbf{w}(T_j)) \cap \text{proj}(O_i) = \emptyset$, it indicates that the obstacle does not overlap with any wheel positions, implying a safe traversal $f_{\text{passable}}(T_j, O_i) = 1$.

Finally, based on $f_{\text{height}}(h_{O_i}, h_v)$ and $f_{\text{wheel}}(T_j, O_i)$, we can define the function $f_{\text{crossable}}(T_j, O_i)$ to evaluate whether the ego vehicle can safely cross an obstacle:

$$f_{\text{crossable}}(T_j, O_i) = f_{\text{height}}(h_{O_i}, h_v) \times f_{\text{wheel}}(T_j, O_i), \quad (35)$$

where $f_{\text{crossable}}(T_j, O_i)$ is a binary variable, in which “0” indicates it cannot be crossed, and “1” indicates it can be safely crossed. $f_{\text{crossable}}(T_j, O_i) = 1$ when the obstacle does not collide with the vehicle’s chassis or wheels.

2) *Obstacle Handling in 4WIS Hybrid A**: We propose a hierarchical obstacle handling strategy for the node expansion process, as illustrated in Fig. 9. First, we determine whether the obstacle is crossable. If the node can directly cross the obstacle without collisions, the node expansion chooses to “cross” the obstacle, and the process terminates. Otherwise, we assess whether the obstacle can be driven over. If “Yes”, it chooses to “drive-over” the obstacle, and the process terminates. However, if neither crossing nor driving over is possible, we test for avoidance. If there exist available free spaces allowing the node to avoid the obstacle, it chooses to “avoid” the obstacle and the process terminates. Finally, if none of the above conditions are met, the node expansion process fails. The process can be formulated as

$$\text{ObstacleHandling}(n_c) = \begin{cases} \text{True}, & \text{succeeds,} \\ \text{False}, & \text{fails.} \end{cases} \quad (36)$$

where $\text{ObstacleHandling}(n_c)$ denotes the result of node expansion at node n_c , with *True* indicating a successful expansion and *False* indicating a failure.

C. Initial Path Generation

With the proposed 4WIS hybrid A*, an initial path can be generated for the OCP. In Algorithm 1, given the initial state X_s , goal state X_f , and scene image I , the scene complexity is assessed using the multimodal classification network function $f_{\text{mcn}}(X_s, X_f, I)$ (line 3). If the scene is classified as the “Hard” task, the guided point set $G = \{g_i\}_{i=1}^N$ and the corresponding key point set $Q = \{q_i\}_{i=1}^{N_q}$, where $Q = \{X_s, g_1, g_2, \dots, g_N, X_f\}$, are employed. In this case, the improved 4WIS hybrid A* algorithm (Algorithm 2) is used to generate a path segment S_i from g_i to a downstream key point in Q (line 8). If $S_i \neq \emptyset$, indicating a successful segment generation, the segment is appended to construct the complete path S , and the key point index is updated for the next iteration. If $S_i = \emptyset$, the process terminates and pathfinding fails. Conversely, if the scene is classified as the “Easy” task, the initial path S is directly generated using 4WISHybridAstar() (see Algorithm A.2 in Appendix).

Algorithm 1 Initial Path Generation

```

1: Input: Initial state  $X_s$ , goal state  $X_f$ , and scene image  $I$ .
2: Initialize: initial path  $\mathcal{S} \leftarrow \emptyset$ ,  $m \leftarrow 1$ ,  $i \leftarrow 1$ .
3: Compute scene_complexity  $\leftarrow f_{\text{mcn}}(X_s, X_f, I)$ .
4: if scene_complexity == "Hard" then
5:   Generate guided points  $G$  and key points  $Q = \{q_i\}_{i=1}^{N_q}$ ;
6:   while  $i < N_q$  do
7:     Select one key point  $q_i$  from  $Q$ ;
8:      $\mathcal{S}_i, m \leftarrow \text{Improved4WISHybridAstar}(i, q_i, Q)$ ;
9:     if  $\mathcal{S}_i = \emptyset$  then
10:      break // Task fails.
11:    end if
12:    Append segmented path  $\mathcal{S} \leftarrow \mathcal{S} \cup \mathcal{S}_i$ ;
13:    Update key points index;  $i \leftarrow m$ 
14:  end while
15: else if then
16:    $\mathcal{S} \leftarrow \text{4WISHybridAstar}(X_s, X_f)$ ; // Easy task.
17: end if
18: Output: initial path  $\mathcal{S}$ 
  
```

With the guided points, the improved 4WIS hybrid A* algorithm (Algorithm 2) takes the key point index i , the corresponding key point q_i , and the key points set Q as inputs. The algorithm first attempts to directly connect q_i to q_{i+1} (line 3) using either a Reeds–Shepp path or a straight-line segment. If $\text{TrajConnect}(q_i, q_{i+1}) \neq \emptyset$, the resulting path and the updated key point index $m = i + 1$ are returned, and the procedure terminates. When a direct connection is not feasible, the algorithm proceeds by expanding the node from q_i . The key point q_i is added to the open set O , and its cost $F(q_i)$ is stored in the cost set \mathcal{F} . While the open set O is not empty and the maximum number of iterations has not been reached, the following steps are performed. The node n_p with the lowest cost is selected from O (line 8), removed from the open set, and added to the closed set C . Then, expansion is performed by generating a successor node n_c using an action $a \in M_s$, where M_s denotes the set of motion modes available to 4WIS vehicles. During the expansion process, the hierarchical obstacle-handling strategy is applied via $\text{ObstacleHandling}(\cdot)$ (line 12) to evaluate traversability. When a feasible expansion node n_c is generated. The algorithm then attempts to connect n_c to a downstream key point $q_m \in \{q_{N_q}, \dots, q_{i+1}\}$ (line 17) to construct a valid path. For example, if a connection is established from n_c to q_{i+2} , a forward path \mathcal{S}_{con} is generated. Subsequently, a backward path $\mathcal{S}_{\text{back}}$ from q_i to n_c is constructed (line 21). The resulting segmented path \mathcal{S}_{seg} , connecting q_i to q_{i+2} , is obtained by concatenating $\mathcal{S}_{\text{back}}$ and \mathcal{S}_{con} . Finally, the algorithm returns \mathcal{S}_{seg} along with the updated key point index $m = i + 2$, as shown in Fig. 10. If no valid downstream connections can be established from n_c using any motion mode of the 4WIS vehicle, the algorithm continues by expanding a new node n_c from the current node and repeating the loop (line 10) until either a feasible key point q is found or the maximum iteration is reached.

VI. COLLISION CONSTRAINTS FORMULATION

A. Collision Constraints of Dynamic Obstacles

1) **Probabilistic Risk Field Model:** We design a driving risk field model to quantify the driving risks caused by dynamic

Algorithm 2 Improved4WISHybridAstar

```

1: Input: Current index  $i$ , key point  $q_i$ , key point set  $Q$ .
2: Initialize: Open set  $O \leftarrow \emptyset$ , closed set  $C \leftarrow \emptyset$ ,  $j \leftarrow 1$ , cost set  $\mathcal{F} \leftarrow \emptyset$ , segment path  $\mathcal{S}_{\text{seg}} \leftarrow \emptyset$ .
3: if  $\text{TrajConnect}(q_i, q_{i+1}) \neq \emptyset$  then
4:   return  $\text{TrajConnect}(q_i, q_{i+1})$ ,  $i + 1$ 
5: end if
6: Add  $q_i$  to the open set  $O$ , add  $F(q_i)$  into the cost set  $\mathcal{F}$ ;
7: while  $O \neq \emptyset$  and  $j \leq \text{MaxIteration1}$  do
8:    $n_p \leftarrow \text{FindMinCostNode}(O, \mathcal{F})$ ; //  $n_p \in O$  minimum cost.
9:   Remove  $n_p$  from open set  $O$  and add to close set  $C$ ;
10:  for action  $a$  in the motion sets  $M_s$  do
11:    Expand node  $n_c$  from  $n_p$  with action  $a$  using (1), (2), (3);
12:    if  $n_c \in C$  or  $\text{ObstacleHandling}(n_c)$  in (36) is FALSE then
13:      continue; // Skip invalid or colliding node.
14:    end if
15:    Compute the node cost  $F(n_c)$  using (28);
16:    Add  $n_c$  to open set  $O$ , add  $F(n_c)$  to cost set  $\mathcal{F}$ ;
17:    for  $m$  in  $\{N_q, N_q - 1, \dots, i + 1\}$  do
18:      Select  $q_m$  from key points set  $Q$ ;
19:       $\mathcal{S}_{\text{con}} \leftarrow \text{TrajConnect}(n_c, q_m)$ ; // path from  $n_c$  to  $q_m$ .
20:      if  $\mathcal{S}_{\text{con}} \neq \emptyset$  then
21:         $\mathcal{S}_{\text{back}} \leftarrow \text{BackTracking}(n_c, q_i)$ ; // Backward path from  $q_i$  to  $n_c$ .
22:         $\mathcal{S}_{\text{seg}} \leftarrow \mathcal{S}_{\text{back}} + \mathcal{S}_{\text{con}}$ ; // path  $q_i$  to  $q_m$ .
23:        return  $\mathcal{S}_{\text{seg}}$ ,  $m$ 
24:      end if
25:    end for
26:  end for
27:   $j \leftarrow j + 1$ ;
28: end while
29: Output: Segmented path  $\mathcal{S}_{\text{seg}}$ , index  $m$ 
  
```

obstacles with motion uncertainties. This section takes the pedestrian as an example for the risk modeling. There are $N_p \in Z^+$ pedestrians in the environment, and the constant acceleration model is used for pedestrians:

$$\begin{cases} x^{p,n}(k+1) = x^{p,n}(k) + v_x^{p,n}(k)\Delta t + \frac{1}{2}a_x^{p,n}(k)\Delta t^2, \\ y^{p,n}(k+1) = y^{p,n}(k) + v_y^{p,n}(k)\Delta t + \frac{1}{2}a_y^{p,n}(k)\Delta t^2, \end{cases} \quad (37)$$

where $x^{p,n}(k)$ and $y^{p,n}(k)$ represent the longitudinal and lateral positions of the n -th ($n \in [1, N_p]$) pedestrians. $v_x^{p,n}(k), v_y^{p,n}(k), a_x^{p,n}(k), a_y^{p,n}(k)$ denote the longitudinal velocity, lateral velocity, longitudinal acceleration, and lateral acceleration, respectively. Δt is the time interval. Considering motion uncertainties, we define the variances of the pedestrian's position as

$$\mathbf{D}^{p,n}(k) = \begin{bmatrix} \text{Var}(x^{p,n}(k)) & 0 \\ 0 & \text{Var}(y^{p,n}(k)) \end{bmatrix}, \quad (38)$$

where $\mathbf{D}^{p,n}(k)$ is the covariance matrix, $\text{Var}(x^{p,n}(k))$ and $\text{Var}(y^{p,n}(k))$ are the variances of longitudinal and lateral

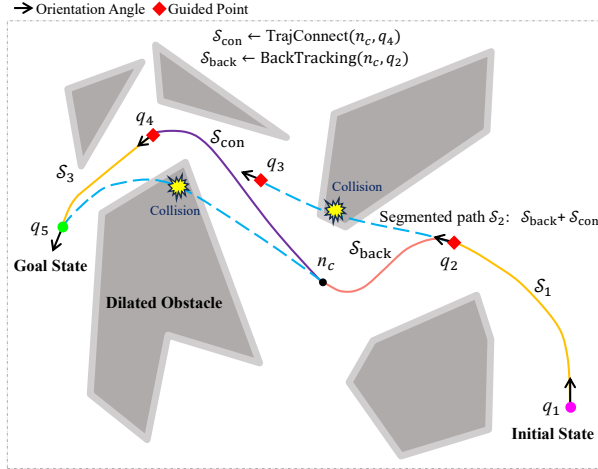


Fig. 10. Initial path generation is performed using Algorithm 1 and Algorithm 2. It first establishes a successful direct connection from q_1 to q_2 . It then attempts to connect q_2 to q_3 , but this is found to be infeasible due to collisions. To address this, a node n_c is expanded from q_2 , and a connection to q_5 is attempted; however, this path fails. It then tries connecting n_c to q_4 , which results in a feasible forward path, denoted as \mathcal{S}_{con} . A backward path $\mathcal{S}_{\text{back}}$ from q_2 to n_c is subsequently constructed. By concatenating $\mathcal{S}_{\text{back}}$ and \mathcal{S}_{con} , the trajectory segment \mathcal{S}_2 , connecting q_2 to q_4 , is obtained. In the next iteration, node expansion continues from q_4 , and a direct connection to the goal node q_5 successfully generates the segment \mathcal{S}_3 . Finally, the segments \mathcal{S}_1 , \mathcal{S}_2 , and \mathcal{S}_3 are concatenated to construct the complete initial path.

positions:

$$\left\{ \begin{array}{l} \text{Var}(x^{p,n}(k)) = \sigma_x^2 + \sum_{i=1}^k \left(\Delta t^2 (\sigma_{vx}^2 + (\sigma_{ax}^n(i))^2 \Delta t^2) + \frac{(\sigma_{ax}^n(i))^2 \Delta t^4}{4} \right), \\ \text{Var}(y^{p,n}(k)) = \sigma_y^2 + \sum_{i=1}^k \left(\Delta t^2 (\sigma_{vy}^2 + (\sigma_{ay}^n(i))^2 \Delta t^2) + \frac{(\sigma_{ay}^n(i))^2 \Delta t^4}{4} \right), \end{array} \right. \quad (39)$$

where σ_x^2 and σ_y^2 are the initial position variances along x-axis and y-axis, σ_{vx}^2 and σ_{vy}^2 are velocity variances, and $(\sigma_{ax}^n(i))^2$ and $(\sigma_{ay}^n(i))^2$ are the acceleration variances at the sampling time i , respectively.

We construct a continuous risk potential field to quantify collision risk, where the Mahalanobis distance [32] is used to evaluate the standardized spatial relationship between the vehicle and each pedestrian:

$$d_M^n(k) = \sqrt{(\mathbf{r}^n)^\top (\mathbf{D}^{p,n}(k))^{-1} \mathbf{r}^n}, \quad \mathbf{r}^n = \begin{bmatrix} x(k) - x^{p,n}(k) \\ y(k) - y^{p,n}(k) \end{bmatrix}, \quad (40)$$

where $d_M^n(k)$ denotes the Mahalanobis distance between the vehicle position $(x(k), y(k))$ and the predicted position of the n -th pedestrian at time k . Referring to [33] and [34], the driving risk field model is formulated as

$$U^{p,n}(k) = \begin{cases} \alpha \left(\frac{1}{d_M^n(k)} - \frac{1}{d_s} \right)^2 \cdot \frac{1}{|\mathbf{r}^n(k)|} \cdot e^{-\beta v_r}, & d_M^n(k) \leq d_s, \\ 0, & d_M^n(k) > d_s, \end{cases} \quad (41)$$

where $U^{p,n}(k)$ denotes the driving risk field value at time k , d_s is the safety distance, α and β are the constant coefficients, v_r is the relative velocity.

The overall instantaneous risk potential field at time k is then computed by aggregating pedestrians:

$$U^p(k) = \max_{1 \leq n \leq N_p} U^{p,n}(k), \quad (42)$$

where $U(k)$ represents the maximum potential risk.

2) Collision Constraints with Driving Corridor: Considering motion uncertainties, we construct the driving corridor for dynamic obstacles based on the driving risk field model designed above. The driving corridor is then utilized to formulate the linear constraints within the OCP in (7). The driving corridor of the dynamic obstacle at the sampling point $(x(j), y(j))$ can be efficiently obtained in the same way as described in Section II. For each sampling point $(x(j), y(j))$, we require that the potential risks within the driving corridor remain below a predefined threshold $\epsilon_{\text{threshold}}$. If the driving risk is higher than the safe threshold, we adjust the driving corridor until it satisfies safety requirements. $\mathcal{E}_j^{\text{up}}$ is the upper boundary of the driving corridor at point $(x(j), y(j))$. We set M sampling points uniformly along the boundary $\mathcal{E}_j^{\text{up}}$, and each point is denoted as $(x_{\mathcal{E}_j^{\text{up}}}^m, y_{\mathcal{E}_j^{\text{up}}}^m)$, $1 \leq m \leq M$ and the driving risk of the position is denoted by $U_{\mathcal{E}_j^{\text{up}}}^{m,p}$, which is computed using (42).

When the driving risk exceeds the safety threshold $\epsilon_{\text{threshold}}$, the expansion length l_j^{up} in the upward direction $\mathcal{E}_j^{\text{up}}$ is iteratively reduced until the safety condition is met. This adjustment process can be described as follows:

$$l_j^{\text{up}}(z+1) = \begin{cases} l_j^{\text{up}}(z) - \Delta l, & \text{if } U_{\mathcal{E}_j^{\text{up}}}^{m,p} > \epsilon_{\text{threshold}}, \\ l_j^{\text{up}}(z), & \text{otherwise,} \end{cases} \quad (43)$$

where $l_j^{\text{up}}(z)$ denotes the expansion length in the upward direction at the z -th iteration, Δl representing the step size. The expansion lengths in the other directions can be computed in a similar manner. Based on this, the safe driving corridor \mathcal{C}_j^{ϵ} centered at the point $(x(j), y(j))$ can be constructed to ensure that the driving risk remains below the safety threshold. The corresponding linear collision avoidance constraints based on the safe corridor \mathcal{C}_j^{ϵ} can then be formulated as follows:

$$\left\{ \begin{array}{l} \mathcal{E}_{\epsilon,j}^{\text{left}} \leq x(j) \leq \mathcal{E}_{\epsilon,j}^{\text{right}}, \\ \mathcal{E}_{\epsilon,j}^{\text{down}} \leq y(j) \leq \mathcal{E}_{\epsilon,j}^{\text{up}}, \end{array} \right. \quad (44)$$

where $\mathcal{E}_{\epsilon,j}^{\text{left}}$, $\mathcal{E}_{\epsilon,j}^{\text{right}}$, $\mathcal{E}_{\epsilon,j}^{\text{down}}$, and $\mathcal{E}_{\epsilon,j}^{\text{up}}$ denote the left, right, lower, and upper boundaries of the safe corridor \mathcal{C}_j^{ϵ} , respectively, where $j = 0, 1, \dots, N_f$. The collision avoidance constraints are included in the OCP in Section II. By incorporating the driving risk field model, we aim to improve the robustness of the OCP framework, considering the motion uncertainties caused by dynamic obstacles.

B. Logical Constraints of Drive-Over Obstacles

As discussed previously, the “drive-over” obstacles, such as puddles, speed bumps, and cardboard boxes, can be driven over at low speeds. To enforce appropriate speed constraints

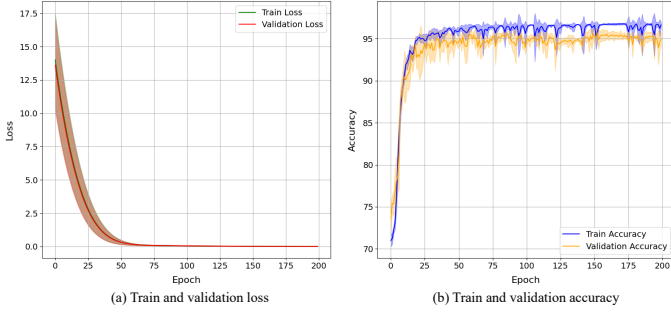


Fig. 11. Training and validation performance. (a) Loss. (b) Accuracy.

when navigating these obstacles, we introduce logical constraints within the OCP framework in (7):

$$\chi_{\text{area}}(x(j), y(j)) \times \varsigma(v(j)) = 0, j = 0, 1, 2, \dots, N_f, \quad (45)$$

where $x(j)$ and $y(j)$ are the vehicle's position at the j -th sample point along its trajectory, the function $\chi_{\text{area}}(x(j), y(j))$ serves as an indicator, returning 1 if the vehicle is driving through "drive-over" obstacle region and 0 otherwise. $\varsigma(v(j))$ is the constraint on the vehicle's velocity. Notably, the constraint in (45) is activated only when $\chi_{\text{area}}(x(j), y(j)) = 1$, *i.e.*, when the vehicle is traversing the "drive-over" obstacles.

The indicator function $\chi_{\text{area}}(x(j), y(j))$ is formulated as

$$\chi_{\text{area}}(x(j), y(j)) = \begin{cases} 1, & \text{if } x(j) \in [x_o^l, x_o^u], y(j) \in [y_o^l, y_o^u], \\ 0, & \text{otherwise,} \end{cases} \quad (46)$$

where x_o^l, x_o^u are the lower and upper bounds of the obstacle region along the x-axis, and y_o^l, y_o^u are the corresponding bounds along the y-axis. $x(j) \in [x_o^l, x_o^u], y(j) \in [y_o^l, y_o^u]$, indicates that the vehicle's current position lies within the specified obstacle region. The vehicle's speed constraint $\varsigma(v(j))$ is formulated as

$$\varsigma(v(j)) = \max \{0, \max (v(j) - v_{\text{ub}}, v_{\text{lb}} - v(j))\}, \quad (47)$$

where v_{lb} and v_{ub} are the lower bound and upper bound of the allowable speed range. This function evaluates to zero when the vehicle's speed $v(j)$ is within the permissible range $[v_{\text{lb}}, v_{\text{ub}}]$ and yields a positive value proportional to the extent of the violation otherwise. This expression enforces that the vehicle's speed lies within the allowable interval $[v_{\text{lb}}, v_{\text{ub}}]$ while navigating through the region of "drive-over" obstacles. By integrating the logical constraints (45) into the OCP in (7), we ensure that the vehicle maintains appropriate speeds when traversing "drive-over" obstacles, thereby enhancing safety and compliance with operational guidelines.

VII. EXPERIMENT RESULTS

A. Implementation Details

Training Details. We collect 2,880 planning task samples, each with randomly assigned obstacles, initial states, and goal states. Each task is solved using the 4WIS hybrid A* algorithm with and without guided points. We compute the success rates and computational costs of both methods to facilitate data labeling. If the 4WIS hybrid A* algorithm without guided

points succeeds and requires less computation time, we label the task as an easy planning task; otherwise, we categorize it as a hard planning task. The dataset is divided into training, validation, and test subsets in an 8:1:1 ratio. Model training is conducted over 200 epochs using five different random seeds. We employ the Adam optimizer with a learning rate of 0.00001 and a batch size of 32. All experiments are conducted on an NVIDIA GeForce RTX 3090 GPU.

Test Scenarios. To assess the performance of the proposed methods across varying levels of scenario complexity, we construct a series of test scenarios categorized by obstacle density: low (5 obstacles), medium (7 obstacles), and high (9 obstacles). Each category encompasses 50 distinct scenarios, and there are 150 test scenarios for evaluation. For each scenario, obstacles are randomly generated as convex polygons with 4 to 7 vertices, and their positions are uniformly distributed within a 40 m \times 40 m workspace. The area of each obstacle is randomly sampled from a uniform distribution ranging between 5 m² and 50 m². Similarly, the initial and goal states are independently and uniformly sampled within the workspace. The orientation angles for both states are sampled from a uniform distribution over the interval $[-\pi, \pi]$, more details are shown in Table A.1 (see Appendix).

B. Training Performance

The training process of the proposed multimodal classification network is illustrated in Fig. 11. As shown in Fig. 11(a), both the training and validation losses decrease sharply within the first 50 epochs and converge to near-zero values, indicating effective learning and stable optimization. In Fig. 11(b), both training and validation accuracies rise rapidly and stabilize after approximately 50 epochs, consistently maintaining values above 95%. These results demonstrate the effectiveness and stability of the proposed multimodal classification network in accurately distinguishing between hard and easy planning tasks. With the well-trained multimodal classification network, our model can identify hard planning tasks and assign guided points to enhance the search efficiency of the 4WIS hybrid A* algorithm. In contrast, for easy planning tasks, guided points are omitted to reduce unnecessary computation time.

C. Comparative Study

This section evaluates the effectiveness of the proposed trajectory planning framework for 4WIS vehicles. We note that all results presented in this section are obtained by first generating an initial path, followed by an optimization process. In the comparative study, a total of 150 scenarios that can be solved by the hybrid A* algorithm are selected, where randomly placed "crossable" and "drive-over" obstacles of varying shapes and sizes are introduced along the generated path to increase task complexity. Additionally, dynamic obstacles such as pedestrians are randomly included to simulate realistic dynamic environments. The trajectory performances of our method are compared against two baseline methods, *i.e.*, Hybrid A* [10] and FTHA [11], as summarized in Table I. Our method consistently outperforms both baselines across all metrics. It achieves the highest success rate of 85.33%,

TABLE I
COMPARISON OF PLANNING RESULTS OF OUR METHOD (FULL MODEL) AND TWO BASELINE METHODS REGARDING 150 SCENARIOS.

Method	Success Rate (%) \uparrow	Path Length (m) \downarrow	Traversal Time (s) \downarrow	Maximum Jerk (m/s 3) \downarrow	Average Jerk (m/s 3) \downarrow	Computation Time (s) \downarrow	Cumulative Risk Potential \downarrow
Hybrid A* [10]	55.33	36.623	33.503	0.474	0.364	40.817	7.590
FTHA [11]	70.67	36.223	33.123	0.437	0.318	42.731	7.284
Ours (Full)	85.33	36.121	32.545	0.408	0.278	26.803	4.119

Note: the baseline methods listed above first generate the initial path, and then subsequently are optimized by the optimal control problem (OCP).

TABLE II
RESULTS OF 4WIS HYBRID A* WITH/WITHOUT GUIDED POINTS (GP).

Method	Success Rate (%)	Path Length (m)	Traversal Time (s)	Computation Time (s)	Maximum Jerk (m/s 3)	Average Jerk (m/s 3)
4WIS Hybrid A*	80%	29.482	41.845	35.630	0.495	0.332
4WIS Hybrid A*+GP	90%	21.570	36.593	25.487	0.433	0.236

Note: all methods generate initial paths, and then are optimized by OCP.

significantly exceeding that of hybrid A* (55.33%) and FTHA (70.67%). It also produces the shortest path length (36.121 m) and traversal time (32.545 s), demonstrating superior path efficiency. In terms of motion smoothness, our method achieves the lowest maximum jerk (0.408 m/s 3) and average jerk (0.278 m/s 3), enabling safer and more comfortable maneuvers. Moreover, our method has achieved the shortest computation time (26.803 s), indicating superior computational efficiency. Notably, our method reduces the cumulative risk potential to 4.119, significantly lower than hybrid A* (7.590) and FTHA (7.284), highlighting its enhanced safety in dynamic and cluttered environments.

D. Validation of Multimodal Classification Network and Guided Points

1) *Guided Points:* We first evaluate the effectiveness of the guided point in our method. We compare the trajectory performance of the 4WIS hybrid A* algorithm with and without the guided point using 50 randomly selected planning tasks, as shown in Table II, which demonstrates the effectiveness of guided points in trajectory planning. With guided points, our method demonstrates a notable performance improvement, achieving a higher success rate (90% vs. 80%), while significantly reducing the path length (from 29.482 m to 21.570 m) and traversal time (from 41.845 s to 36.593 s). Additionally, the computation time has been reduced by more than 10 seconds. The generated trajectories are also smoother, as evidenced by the reductions in maximum jerk (0.433 m/s 3 vs. 0.495 m/s 3) and average jerk (0.236 m/s 3 vs. 0.332 m/s 3). These results show the effectiveness of guided points in improving travel efficiency, smoothness of the trajectories, and computational efficiency.

2) *Multimodal Classification Network:* Then, we evaluate the impact of the multimodal classification network in our method. The multimodal classification network is expected to improve computational efficiency by determining the necessity of guided points based on the scenario's complexity. We evaluate the computation time of the 4WIS hybrid A* algorithm with and without the multimodal classification network using 50 randomly selected planning tasks, as shown in Table III. With the multimodal classification network, the computation

TABLE III
COMPARATIVE RESULTS OF 4WIS HYBRID A*+GUIDED POINTS (GP) WITH/WITHOUT MULTIMODAL CLASSIFICATION NETWORK (MCN).

Method	Computation Time (s) \downarrow
4WIS Hybrid A*+GP	46.848
4WIS Hybrid A*+MCN+GP	38.166

Note: all methods generate initial paths, and then are optimized by OCP.

time decreases from 46.848 s to 38.166 s, resulting in an approximate 18.5% improvement in computational efficiency, showing the effectiveness of this module.

3) *Multimodal Classification Network and Guided Points:* This section validates the effectiveness of the integration of the multimodal classification network and the guided points, and chooses hybrid A* [10] and FTHA [11] as baseline methods. The experiments are conducted across three obstacle density levels: low, medium, and high, as summarized in Table IV. Our method consistently outperforms both baselines across all metrics in medium and high density scenarios. Considering the success rate, our method consistently outperforms hybrid A* and FTHA in terms of the success rate metric across all obstacle densities. Specifically, it achieves a 100% success rate in low-density environments and significantly higher success rates in medium (84%) and high density (82%) scenarios compared to hybrid A* (42%, 38%) and FTHA (64%, 68%). Regarding path length and traversal time, our method demonstrates superior performance in medium and high-density settings. While hybrid A* shows advantages in travel efficiency in low-density environments, our method achieves comparable performance, indicating its path efficiency. Additionally, our approach ensures the smoothest trajectories, exhibiting the lowest maximum and average jerk values across all environments. In terms of computation time, our method achieves the minimum in medium and high-density scenarios (34.481 s and 23.156 s, respectively) and maintains comparable efficiency to hybrid A* in low-density scenarios (9.727 s vs. 9.945 s).

Fig. 12 demonstrates that all methods can generate feasible trajectories in low-density scenarios, with our approach achieving computation times comparable to hybrid A*. In medium-density environments, hybrid A* fails to produce feasible paths, while FTHA can find a path but requires significantly more computation time. In high-density scenarios, FTHA's optimization process fails due to violating the vehicle's kinematic constraints. In contrast, our method consistently generates high-quality initial paths that adhere to kinematic constraints, ensuring successful optimization across all obstacle densities.

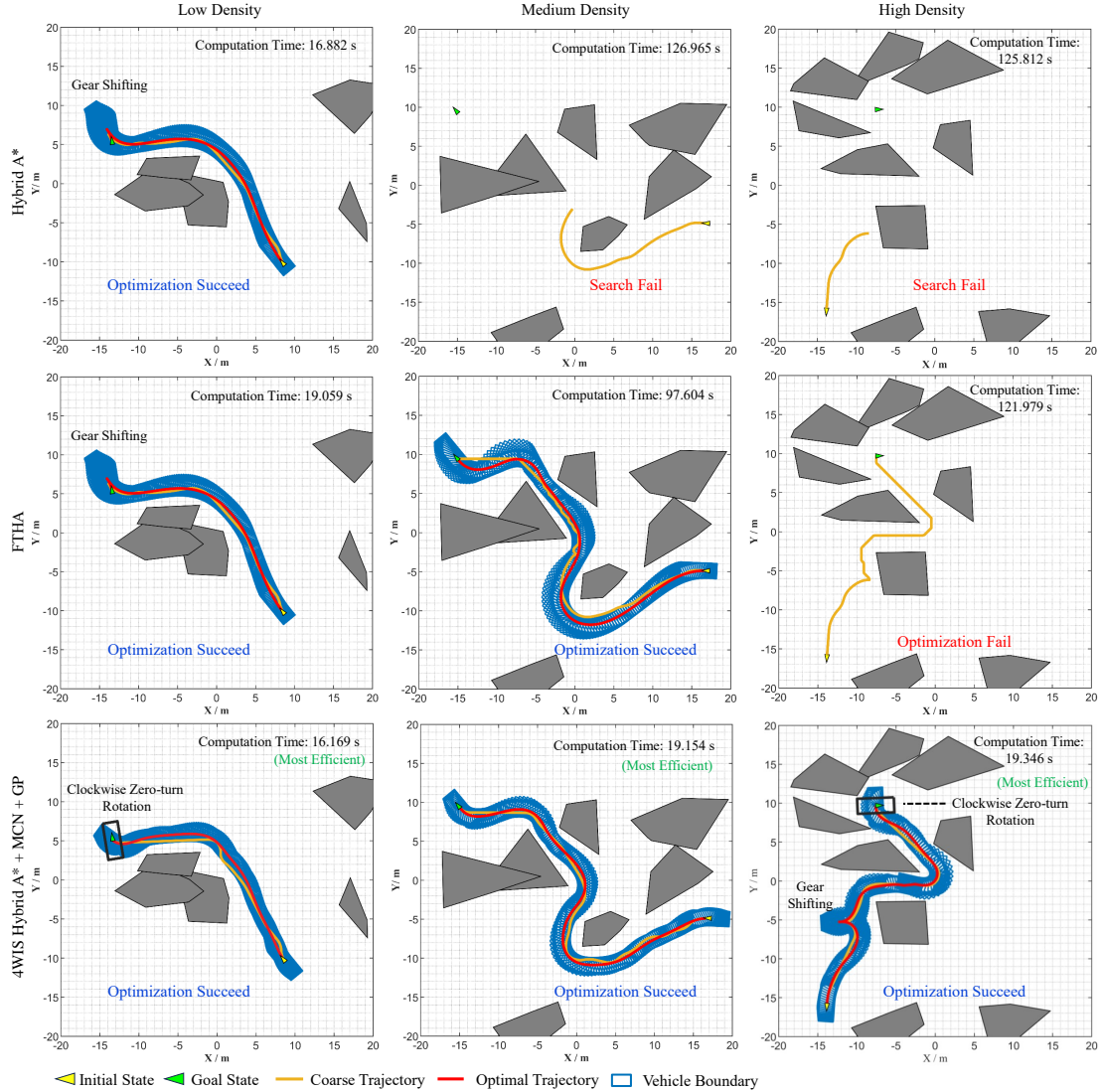


Fig. 12. Visualization of the 4WIS hybrid A* algorithm enhanced with a Multimodal Classification Network (MCN) and Guided Points (GP) across low-, medium-, and high-density obstacle scenarios. The baseline hybrid A* algorithm (top row) succeeds only in low-density environments and fails as obstacle density increases. The FTHA method (middle row) generates optimized trajectories under low and medium densities but fails to optimize under high-density conditions. In contrast, our 4WIS hybrid A* with MCN and GP consistently generates feasible trajectories across all density levels. These results highlight the effectiveness of the proposed MCN and GP.

E. Validation of Hierarchical Obstacle Handling Strategy

1) *Crossable Obstacle*: The effectiveness of the “Crossable” Obstacle Handling Strategy (COHS) is evaluated. We selected 50 scenarios that can be solved by the 4WIS hybrid A* algorithm and introduced randomly placed “crossable” obstacles of varying shapes and sizes to increase task complexity. We then compared the trajectory performance of the 4WIS hybrid A* algorithm with and without the proposed “crossable” obstacle handling strategy, as summarized in Table V. The proposed method achieves a success rate of 92%, significantly higher than the 70% of 4WIS hybrid A*. It also outperforms in terms of path length (26.872 m vs. 28.325 m) and traversal time (22.860 s vs. 23.219 s), indicating improved path efficiency. Furthermore, it yields lower maximum jerk (0.498 m/s^3) and average jerk (0.348 m/s^3), resulting in smoother and more comfortable trajectories. Although it incurs a slight increase in computation time, the proposed method demonstrates substantial improvements in

success rate, path efficiency, and path smoothness.

Fig. 13 illustrates two examples of the trajectory planning results for 4WIS hybrid A* and the proposed method in environments containing “crossable” obstacles. In Case 1, 4WIS hybrid A* conservatively avoids all obstacles, including “crossable” ones, resulting in a longer path (42.82 m) and higher computation time (32.204 s). In contrast, the proposed method efficiently navigates narrow regions by traversing the “crossable” obstacles, producing a shorter path (26.63 m) with reduced computation time (14.064 s). In Case 2, 4WIS hybrid A* fails to generate a valid coarse trajectory, while our method successfully computes a feasible and optimized path by exploiting obstacle traversability. These results highlight the proposed method’s superior adaptability and efficiency in constrained environments with “crossable” obstacles.

2) *Drive-Over Obstacle*: The “Drive-over” Obstacles Handling Strategy (DOHS) enables the vehicle to safely traverse obstacles at low speeds. To evaluate its effectiveness, we

TABLE IV
COMPARISON OF TRAJECTORY PLANNING RESULTS 4WIS HYBRID A*+MCN+GP WITH TWO BASELINE METHODS.

		Method	Success Rate (%) \uparrow	Path Length (m) \downarrow	Traversal Time (s) \downarrow	Maximum Jerk (m/s 3) \downarrow	Average Jerk (m/s 3) \downarrow	Computation Time (s) \downarrow
Low density	Hybrid A* [10]	96%	25.324	17.798	0.851	0.389	9.727	
	FTHA [11]	100%	29.003	30.806	0.817	0.318	20.646	
	4WIS Hybrid A*+MCN+GP	100%	26.155	18.292	0.766	0.302	9.945	
Medium density	Hybrid A* [10]	42%	64.934	40.314	0.475	0.292	122.470	
	FTHA [11]	64%	66.558	51.843	0.568	0.285	122.124	
	4WIS Hybrid A*+MCN+GP	84%	47.975	30.323	0.308	0.168	34.481	
High density	Hybrid A* [10]	38%	60.048	69.117	0.483	0.288	87.607	
	FTHA [11]	68%	55.354	38.470	0.745	0.306	75.338	
	4WIS Hybrid A*+MCN+GP	82%	45.499	35.965	0.453	0.192	23.156	

Note: all methods listed above are used to generate the initial path, and then optimized by OCP.

TABLE V
COMPARISON OF PLANNING RESULTS OF 4WIS HYBRID A* WITH AND WITHOUT CROSSABLE OBSTACLE HANDLING STRATEGY (COHS).

Method	Success Rate	Path Length	Traversal Time	Computation Time	Maximum Jerk	Average Jerk
4WIS Hybrid A*+COHS	92%	26.872	22.860	17.603	0.498	0.348
4WIS Hybrid A*	70%	28.325	23.219	15.844	0.527	0.355

Note: all methods listed above are used to generate the initial path, and then optimized by OCP.

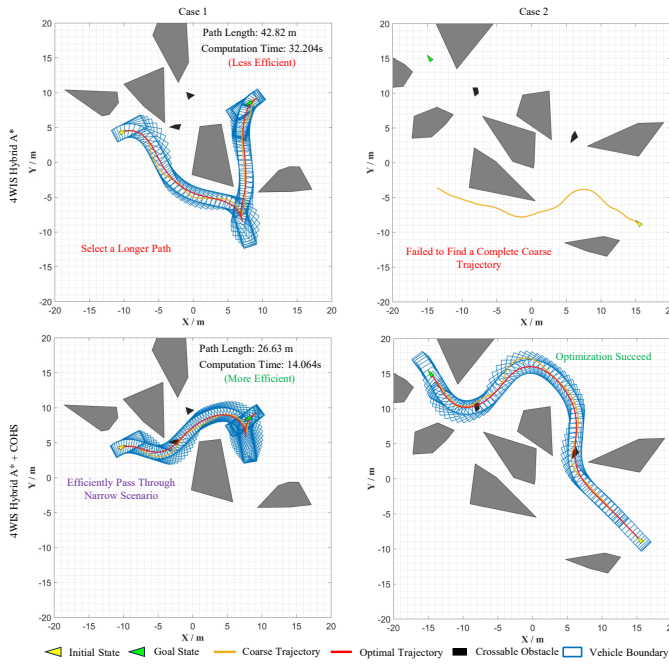


Fig. 13. Visualization of the 4WIS hybrid A* algorithm with and without the “crossable” obstacle handling strategy. In the top row, the planner avoids all obstacles, leading to a longer path in Case 1 and failing to generate a valid path in Case 2. In contrast, the 4WIS hybrid A* algorithm with the crossable obstacle handling strategy (COHS) leverages the traversability of “crossable” obstacles to generate shorter and feasible paths in both cases, demonstrating enhanced path efficiency in constrained environments.

selected 50 scenarios that can be solved by the 4WIS hybrid A* algorithm and introduced randomly placed “drive-over” obstacles of varying shapes and sizes to increase task complexity. We then compared the trajectory performance of the 4WIS hybrid A* algorithm with and without the proposed “drive-over” obstacle handling strategy, as summarized in Table VI. The proposed method achieves a success rate of 90%, significantly higher than the 76% of 4WIS hybrid A*. It also outperforms in path length (23.420 m vs. 27.242 m) and traversal time (24.579 s vs. 25.921 s), demonstrating enhanced

TABLE VI
COMPARISON OF PLANNING RESULTS USING 4WIS HYBRID A* WITH AND WITHOUT DRIVE-OVER OBSTACLE HANDLING STRATEGY (DOHS).

Method	Success Rate (%)	Path Length (m)	Traversal Time (s)	Computation Time (s)	Maximum Jerk (m/s 3)	Average Jerk (m/s 3)
4WIS Hybrid A*+DOHS	90%	23.420	24.579	22.827	0.517	0.361
4WIS Hybrid A*	76%	27.242	25.921	20.968	0.498	0.375

Note: DOHS impacts the node expansion of 4WIS Hybrid A* and velocity optimization in OCP.

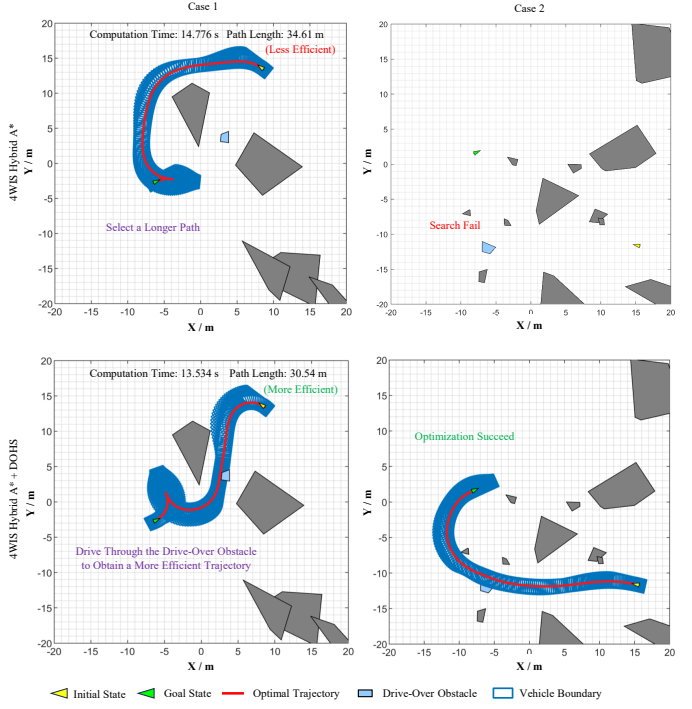


Fig. 14. Visualization of the 4WIS hybrid A* algorithm with and without the “drive-over” obstacle handling strategy. The planner avoids all obstacles, leading to a longer path in Case 1 and a planning failure in Case 2. In contrast, the 4WIS hybrid A* algorithm equipped with the drive-over obstacle handling strategy (DOHS) leverages “drive-over” obstacle properties to generate shorter and feasible trajectories, demonstrating improved planning efficiency in constrained environments.

path efficiency. In addition, the proposed approach yields a lower average jerk (0.361 m/s 3 vs. 0.375 m/s 3) and a comparable maximum jerk (0.517 m/s 3 vs. 0.498 m/s 3), indicating improved trajectory smoothness. While the computation time increases slightly, the strategy delivers notable gains in success rate, path efficiency, and trajectory quality.

Fig. 14 illustrates the trajectory planning results of the 4WIS hybrid A* algorithm and our method in narrow environments containing “drive-over” obstacles. Fig. 14 (a) shows that the

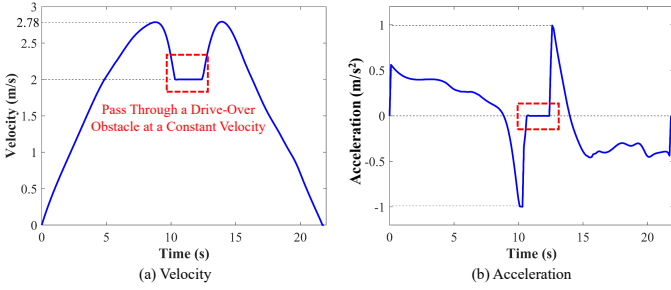


Fig. 15. Vehicle's velocity and acceleration profiles while traversing a "drive-over" obstacle. (a) The vehicle maintains a constant speed of approximately 2 m/s during the traversal period. (b) The acceleration profile remains close to zero during traversal, indicating minimal dynamic disturbance. This demonstrates the vehicle passes slowly over the obstacle to ensure safety.

TABLE VII

COMPARISON OF PLANNING RESULTS USING 4WIS HYBRID A* WITH AND WITHOUT THE RISK FIELD-BASED DRIVING CORRIDOR (RFDC).

Method	Cumulative Risk ↓ Potential	Minimum ↑ Distance (m)	Path ↓ Length (m)	Traversal ↓ Time (s)	Computation ↓ Time (s)
4WIS Hybrid A* + RFDC	3.235	1.591	35.472	25.383	21.177
4WIS Hybrid A*	10.141	0.884	33.414	24.623	22.552

Note: 4WIS Hybrid A* generates initial paths. RFDC generates collision constraints of dynamic obstacles in OCP.

4WIS hybrid A* algorithm detours around each obstacle, while our method chooses to safely drive over the obstacles, reducing the path length by approximately 4 m and the computation time by 1.2 s. Fig. 14 (b) illustrates a more challenging scenario in which the 4WIS hybrid A* fails to generate a feasible path due to the presence of the "drive-over" obstacle, whereas our approach successfully yields an optimal trajectory that safely traverses the obstacle. Furthermore, the velocity and acceleration profiles of Case 2 are illustrated in Fig. 15. The vehicle decelerates and then proceeds at a constant speed of 2.0 m/s with zero acceleration when passing over the "drive-over" obstacle, thereby ensuring safe traversal.

F. Impact of Driving Risk Field-based Driving Corridor

To evaluate the effectiveness of probabilistic risk field-based driving corridors in trajectory planning, we compared the performance of the 4WIS hybrid A* algorithm with and without this safety mechanism. Additionally, we calculated the cumulative risk potentials to assess the safety performance of both methods. As shown in Table VII, our approach yields a cumulative risk potential of 3.235, significantly lower than the 10.141 observed for 4WIS hybrid A*. Furthermore, the minimum distance to obstacles achieved by our method is 1.591 m, notably greater than the 0.884 m of 4WIS hybrid A*, indicating enhanced safety. These results demonstrate that incorporating a probabilistic risk field-based driving corridor significantly improves safety while maintaining comparable efficiency. Although our method results in a slightly longer path and increased traversal time, it achieves improved safety with reduced computation time. An example involving two pedestrians is presented in Fig. 16, where the collision risk heatmap highlights that our method maintains a greater distance from high-risk regions compared to 4WIS hybrid A*, effectively reducing collision risk.

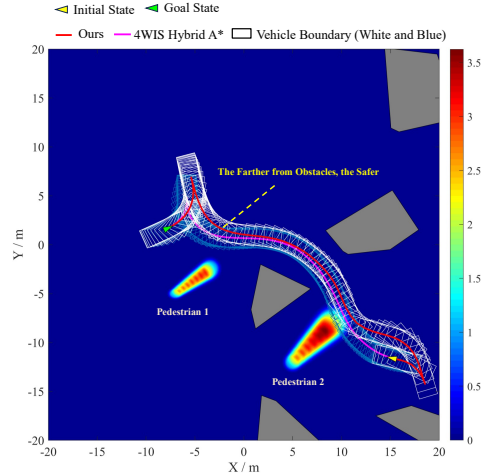


Fig. 16. Visualization of the pedestrian risk field and the planning results of the 4WIS hybrid A* algorithm with and without the risk field-based driving corridor. The 4WIS hybrid A* with the risk field-based driving corridor (RFDC) maintains a greater distance from both static obstacles and dynamic pedestrians, thereby effectively reducing collision risk and enhancing trajectory safety.

VIII. CONCLUSION

This work presents a structurally explainable trajectory planning framework for four-wheel independent steering vehicles in narrow and dynamic environments. Planning decisions are explicitly grounded in obstacle attributes, interpretable motion modes, and transparent safety constraints, enabling human-understandable maneuvering behavior. A multimodal perception module provides semantic scene understanding and guided points for task decomposition, while the 4WIS hybrid A* performs planning through interpretable node expansion and mode selection, and the OCP refines trajectories within this explainable decision structure. A hierarchical obstacle handling strategy establishes a clear mapping between obstacle semantics and planning actions, allowing safe avoidance, crossing, or driving over obstacles. Dynamic obstacles are addressed via a probabilistic risk field formulation to ensure safety with low computational overhead. Experimental results demonstrate that the proposed method achieves safe, efficient, and comfortable trajectory planning with traceable and explainable decision logic. Future work will explore learning-based extensions while preserving interpretability and semantic consistency.

REFERENCES

- [1] J. Guo, Y. Luo, and K. Li, "An adaptive hierarchical trajectory following control approach of autonomous four-wheel independent drive electric vehicles," *IEEE Trans. Intell. Transp. Syst.*, vol. 19, no. 8, pp. 2482–2492, Oct. 2017.
- [2] R. Chen, J. Cheng, Z. Liang, S. Ding, and Z. Yang, "Vehicle motion planning in complex environment via decomposition and convexification," *IEEE Internet Things J.*, vol. 11, no. 7, pp. 12 087–12 101, 2024.
- [3] M.-K. Lu, M.-F. Ge, T.-F. Ding, L. Zhong, and Z.-W. Liu, "Hierarchical piecewise-trajectory planning framework for autonomous ground vehicles considering motion limitation and energy consumption," *IEEE Internet Things J.*, vol. 11, no. 18, pp. 30 145–30 160, 2024.
- [4] Z. Xu, K. Wang, C. Mu, and T. Qiu, "Safety-critical path planning for obstacle avoidance based on reinforcement learning and control barrier functions," *IEEE Internet Things J.*, vol. 12, no. 23, pp. 51 410–51 421, 2025.

- [5] Y. Guo, D. Yao, B. Li, H. Gao, and L. Li, "Down-sized initialization for optimization-based unstructured trajectory planning by only optimizing critical variables," *IEEE Trans. Intell. Veh.*, vol. 8, no. 1, pp. 709–720, Mar. 2022.
- [6] Z. Bai, H. Pang, Z. He, B. Zhao, and T. Wang, "Path planning of autonomous mobile robot in comprehensive unknown environment using deep reinforcement learning," *IEEE Internet Things J.*, vol. 11, no. 12, pp. 22 153–22 166, 2024.
- [7] D. Zhu, Z. Huang, Y. Xiong, C. Wang, and K. Yang, "Centralized mpc-based mixed-integer programming for cooperative trajectory planning in open-pit mines," *IEEE Internet Things J.*, vol. 12, no. 23, pp. 51 064–51 076, 2025.
- [8] A. Nagahama, T. Saito, T. Wada, and K. Sonoda, "Autonomous driving learning preference of collision avoidance maneuvers," *IEEE Trans. Intell. Transp. Syst.*, vol. 22, no. 9, pp. 5624–5634, Apr. 2020.
- [9] D. Fassbender, B. C. Heinrich, and H.-J. Wuensche, "Motion planning for autonomous vehicles in highly constrained urban environments," in *Proc. IEEE/RSJ Int. Conf. Intell. Robots Syst. (IROS)*, 2016, pp. 4708–4713.
- [10] D. Dolgov, S. Thrun, M. Montemerlo, and J. Diebel, "Path planning for autonomous vehicles in unknown semi-structured environments," *Int. J. Rob. Res.*, vol. 29, no. 5, pp. 485–501, Apr. 2010.
- [11] B. Li, T. Acarman, Y. Zhang, Y. Ouyang, C. Yaman, Q. Kong, X. Zhong, and X. Peng, "Optimization-based trajectory planning for autonomous parking with irregularly placed obstacles: A lightweight iterative framework," *IEEE Trans. Intell. Transp. Syst.*, vol. 23, no. 8, pp. 11 970–11 981, Sep. 2021.
- [12] J. Teng, Y. Li, Z. Yang, Z. Yang, X. Shao, and H. Qin, "User preference-aware and efficient trajectory planning for autonomous parking with hybrid a* and nonlinear optimization," in *Proc. 27th Int. Conf. Intell. Transp. Sys. (ITSC)*, 2024, pp. 1090–1097.
- [13] Y. Guo, D. Yao, B. Li, Z. He, H. Gao, and L. Li, "Trajectory planning for an autonomous vehicle in spatially constrained environments," *IEEE Trans. Intell. Transp. Syst.*, vol. 23, no. 10, pp. 18 326–18 336, Apr. 2022.
- [14] C. Sun, Q. Li, B. Li, and L. Li, "A successive linearization in feasible set algorithm for vehicle motion planning in unstructured and low-speed scenarios," *IEEE Trans. Intell. Transp. Syst.*, vol. 23, no. 4, pp. 3724–3736, Jan. 2021.
- [15] B. Li, Y. Ouyang, X. Li, D. Cao, T. Zhang, and Y. Wang, "Mixed-integer and conditional trajectory planning for an autonomous mining truck in loading/dumping scenarios: A global optimization approach," *IEEE Trans. Intell. Veh.*, vol. 8, no. 2, pp. 1512–1522, Oct. 2022.
- [16] X. Liu, W. Wang, X. Li, F. Liu, Z. He, Y. Yao, H. Ruan, and T. Zhang, "Mpc-based high-speed trajectory tracking for 4wids robot," *ISA Trans.*, vol. 123, pp. 413–424, Apr. 2022.
- [17] S. Yoon and D. H. Shim, "Slpa *: Shape-aware lifelong planning a * for differential wheeled vehicles," *IEEE Trans. Intell. Transp. Syst.*, vol. 16, no. 2, pp. 730–740, Aug. 2015.
- [18] Y. Chang, Z. Yang, M. Hu, Y. Bian, and Y. Li, "An optimal parking path planning method integrating motion mode decision-making for 4wids vehicles," in *Proc. 27th Int. Conf. Intell. Transp. Sys. (ITSC)*, 2024, pp. 2570–2577.
- [19] F. Xu, X. Liu, W. Chen, and C. Zhou, "Dynamic switch control of steering modes for four wheel independent steering rescue vehicle," *IEEE Access*, vol. 7, pp. 135 595–135 605, Sep. 2019.
- [20] D. Wang and F. Qi, "Trajectory planning for a four-wheel-steering vehicle," in *Proc. IEEE Int. Conf. Rob. Autom.*, vol. 4, 2001, pp. 3320–3325 vol.4.
- [21] T. L. Lam, H. Qian, and Y. Xu, "Omnidirectional steering interface and control for a four-wheel independent steering vehicle," vol. 15, no. 3, pp. 329–338, Jun. 2010.
- [22] P. Hang, Y. Han, X. Chen, and B. Zhang, "Design of an active collision avoidance system for a 4wids-4wid electric vehicle," *IFAC-PapersOnLine*, vol. 51, no. 31, pp. 771–777, 2018.
- [23] B. Hua, R. Chai, X. Wang, S. Chai, J. Zhang, and Y. Xia, "A lightweight optimal trajectory planning for smart summon in highly complex and irregular parking lot scenarios," *IEEE Trans. Intell. Transp. Syst.*, vol. 25, no. 8, pp. 9192–9203, Feb. 2024.
- [24] J. Lian, W. Ren, D. Yang, L. Li, and F. Yu, "Trajectory planning for autonomous valet parking in narrow environments with enhanced hybrid a* search and nonlinear optimization," *IEEE Trans. Intell. Veh.*, vol. 8, no. 6, pp. 3723–3734, Apr. 2023.
- [25] L. Yang, Q. Wang, Y. Tan, and J. Gong, "Autonomous vehicle path planning considering dwarf or negative obstacles," in *IEEE Intell. Veh. Symp. Proc.*, 2019, pp. 1021–1026.
- [26] C. Park, J. S. Park, and D. Manocha, "Fast and bounded probabilistic collision detection for high-dof trajectory planning in dynamic environments," *IEEE Trans. Autom. Sci. Eng.*, vol. 15, no. 3, pp. 980–991, Mar. 2018.
- [27] Y. Liu, X. Pei, H. Zhou, and X. Guo, "Spatiotemporal trajectory planning for autonomous vehicle based on reachable set and iterative lqr," *IEEE Trans. Veh. Technol.*, vol. 73, no. 8, pp. 10 932–10 947, Feb. 2024.
- [28] W. Xu, J. Pan, J. Wei, and J. M. Dolan, "Motion planning under uncertainty for on-road autonomous driving," in *Proc. IEEE Int. Conf. Robot. Autom. (ICRA)*, 2014, pp. 2507–2512.
- [29] M. Wang, L. Zhang, Z. Zhang, and Z. Wang, "A hybrid trajectory planning strategy for intelligent vehicles in on-road dynamic scenarios," *IEEE Trans. Veh. Technol.*, vol. 72, no. 3, pp. 2832–2847, Oct. 2022.
- [30] S. Li, W. Wang, B. Wang, H. Guan, H. Liu, S. Wu, and H. Chen, "Hierarchical trajectory planning based on adaptive motion primitives and bilevel corridor," *IEEE Trans. Veh. Technol.*, vol. 73, no. 11, pp. 16 238–16 253, Jun. 2024.
- [31] K. He, X. Zhang, S. Ren, and J. Sun, "Deep residual learning for image recognition," in *Proc. IEEE/CVF Conf. Comput. Vis. Pattern Recognit.*, 2016, pp. 770–778.
- [32] Y. Washizawa and S. Hotta, "Mahalanobis distance on extended grassmann manifolds for variational pattern analysis," *IEEE Trans. Neural Networks Learn. Syst.*, vol. 25, no. 11, pp. 1980–1990, 2014.
- [33] J. W. Jian Wu, Yang Li, "The driving safety field based on driver–vehicle–road interactions," *IEEE Trans. Intell. Transp. Syst.*, vol. 16, no. 4, pp. 2203 – 2214, Aug. 2015.
- [34] L. Li, J. Gan, X. Ji, X. Qu, and B. Ran, "Dynamic driving risk potential field model under the connected and automated vehicles environment and its application in car-following modeling," *IEEE Trans. Intell. Transp. Syst.*, vol. 23, no. 1, pp. 1524–9050, Jul. 2020.